博士論文番号 0681024

Structural studies of cytoskeleton-regulating proteins: the radixin-CD44 and EB1-CLASP2γ complexes.
(細胞骨格制御タンパク質の構造生物学的研究：ラデキシン-CD44 ならびに、EB1-CLASP2γ複合体)

奈良先端科学技術大学院大学
バイオサイエンス研究科
生体高分子構造学講座
(構造生物学)

(箱嶋　敏雄　教授)

平成 20 年 12 月 22 日提出

バイオサイエンス研究科　博士論文要旨

所属 （主指導教員）	構造生物学 （箱嶋 敏雄　教授）		
氏名	森　智行	提出	平成 20 年 12 月 22 日
題目	Structural studies of cytoskeleton-regulating proteins: the radixin-CD44 and EB1-CLASP2γ complexes. （細胞骨格制御タンパク質の構造生物学的研究：ラデキシン-CD44 ならびに、EB1-CLASP2γ複合体）		

Abstract

Cytoskeletons such as actin filaments and microtubules play important roles in maintaining cell shape, mediating cell migration and vesicle transport in eukaryotic cells. The purpose of this study is to clarify mechanisms of actions of cytoskeleton-regulating proteins based on their three-dimentional structures. I determined two protein-peptide complexes and clarified details of the intermolecular interactions and the consequences in biological functions.

I. Structural basis for CD44 recognition by ERM (Ezrin/Radixin/Moesin) proteins

CD44 is an important adhesion molecule that specifically binds hyaluronan, a major component of the extracellular matrix, and regulates cell proliferation and motility. Although full activity of CD44 requires binding to ERM proteins that are the linker proteins between the membrane proteins and actin filament, CD44 cytoplasmic region lacks the Motif-1 consensus sequence for binding FERM domain of ERM. Therefore, the precise binding mode of CD44 to the FERM domain remains unknown. I carried out on physicochemical and hydrodynamic analyses of the CD44 cytoplasmic region and determined the crystal structure of the radixin FERM domain complexed with a CD44 juxtamembrane peptide. The crystal structure reveals that the KKKLVIN sequence of the CD44 forms a β strand followed by a short loop structure

that binds subdomain C of the FERM domain. This binding mode resembles that of neutral endopeptidase 24.11 (NEP) rather than ICAM-2. The results reveal acharacteristic versatility of peptide recognition by the FERM domains from ERM proteins, suggest a possible mechanism by which the CD44 tail is released from the cytoskeleton for nuclear translocation by regulated intramembrane proteolysis, and provide a structural basis for Smad1 interactions with activated CD44 bound to ERM protein.

II. Structural studies of the microtubule plus end tracking proteins (+TIPs) and CLASP recognition by EB1

+TIPs specifically recognize the dynamic microtubule (MT) plus ends and regulate MT polymerization-dissociation dynamics at the plus ends with forming protein-protein interaction network. Although +TIPs play a critical role in determination of cell polarity, modes of the MT plus ends recognition by +TIPs and the protein-protein interactions among +TIPs remain unclear. I carried out biochemical and structural studies in an effort to delineate the recognition and interaction modes. I analyzed the interactions among +TIPs containing EB1 (end binding 1) and CLASP2γ (cytoplasmic linker associated protein 2 γ). I showed that EB1 C-terminal domain recognizes 2 repeated region in this Ser/Arg rich region of CLASP. Furthermore, I crystallized the complex between EB1 and CLASP2γ and determined the complex by means of X-ray crystallography. In this complex structure, I found that the Ile side chain of CLASP Ile-Pro motif, which conserved other EB1 targeting proteins such as adenomatous polyposis coli (APC) that is the tumor suppressor gene product, docked into the hydrophobic pocket formed the EB1 C-terminal domain dimmer.

Contents

II. EB1-CLASP complex

II-1. Introduction

II-2. Materials and Methods

II-3. Results

II-4. Discussion

II-5. References

III. Acknowledgments

I. The radixin-CD44 complex

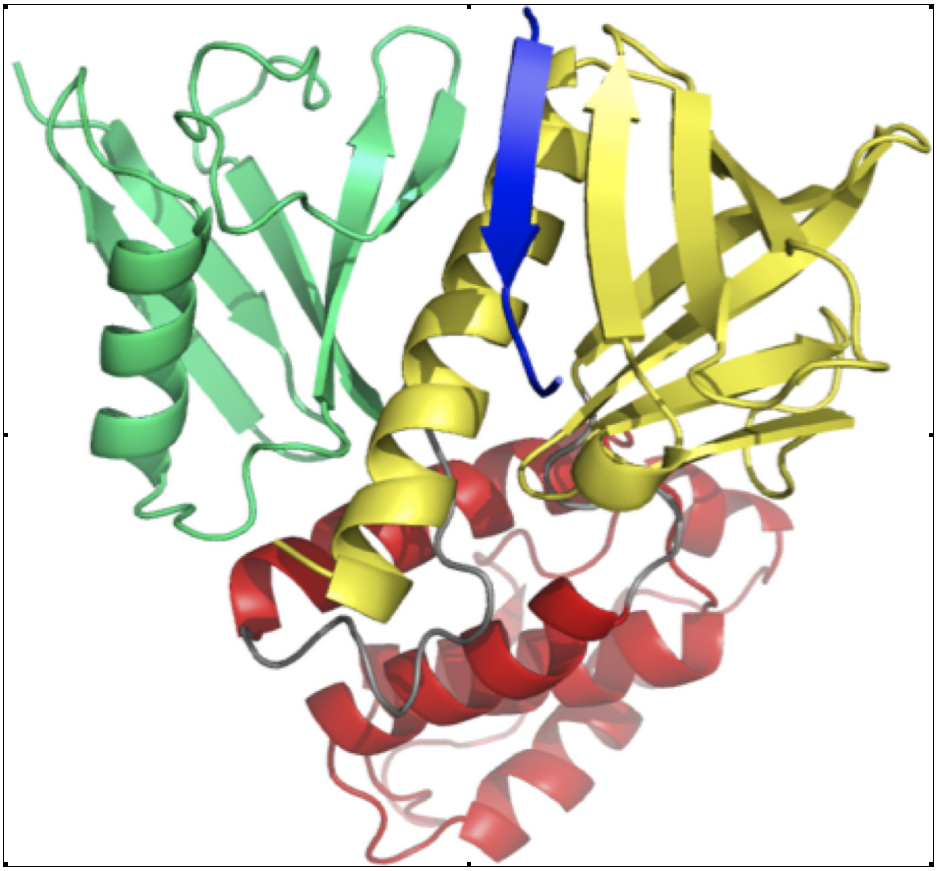

I-1. Introduction

I-1-1. Hyaluronan receptor CD44

Hyaluronan is a major ubiquitous glycosaminoglycan component of the extracellular matrix in vertebrates (1-2). CD44 was the first transmembrane hyaluronan receptor identified, and interest in this receptor stems from the fact that CD44-hyaluronan interactions mediate cell migration in a variety of pathophysiological processes, including tumor metastasis, wound healing, and leukocyte extravasation at inflammation sites (3-6). CD44 and its different isoforms retain the link-homology domain in the extracellular domain for hyaluronan binding and common transmembrane and cytoplasmic regions (Fig. I-1-1) with high sequence conservation among the isoforms and between species (3–4, 7–9).

The CD44 cytoplasmic region, comprising 72 amino acid residues, has been shown to associate with actin filaments in various cells, a process mediated by ERM (ezrin/radixin/moesin) proteins and the closely related protein merlin (also referred to as neurofibromin 2/schwannomin) (10–14), which is the neurofibromatosis type 2 tumor suppressor gene product (15). ERM proteins play a key role as cross-linkers between adhesion molecules on the plasma membrane and actin filaments (13, 16–19). Increasing evidence has shown that interactions between CD44 and ERM proteins are associated with normal physiological cell adhesion and migration functions in addition to bacterial infection and cancer progression (5–6, 20).

Importantly, a minimal cytoplasmic region projecting from a transmembrane helix is required for efficient hyaluronan binding (21–24), probably stabilizing CD44

at the plasma membrane and facilitating receptor clustering. Moreover, these highly conserved transmembrane and cytoplasmic regions are required for events downstream of hyaluronan binding through regulated intramembrane proteolysis (RIP) (25), which produces a CD44 intracellular domain (ICD) fragment that translocates into the nucleus and stimulates transcription via direct interactions with the transcriptional machinery (Fig. I-1-2) (26). However, the physicochemical and structural features of the ICD fragment, which encompasses the whole cytoplasmic region, are unknown.

I-1-2. Ezrin/Radixin/Moesin (ERM) proteins

ERM proteins comprise three domains, an N-terminal globular domain, a central a-helical domain, and a C-terminal tail domain. The N-terminal globular domain is highly conserved (~80 % identity) in ERM proteins and shows 32% identity to equivalent domain in protein 4.1 (Fig. I-1-3). Thus, ERM proteins belong to the protein 4.1 superfamily, which composed of proteins sharing a homology with this domain, called FERM (four point one ERM) domain.

In cytoplasm, ERM proteins are negatively regulated by intramolecular interaction between the FERM domain and C-terminal domain (60-62). The crystallographic study of the moesin FERM domain complexed with the C-terminal domain clarified the molecular basis of this interaction (40). Activation of ERM proteins, which require separation of the FERM domain and C-terminal domain, is regulated by phosphorylation at C-terminal region and lipids, such as phosphatidylinositol 4,5-biphosphate (PIP_2) (64-66). Both signaling pathway

mediated by small GTPase Rho family (11,13). The FERM domain of the activated ERM proteins interacts with the plasma membrane and specifically binds a variety of adhesion molecules, including CD44, whereas the C-terminal tail domain binds to F-actin (Fig. I-1-4). However, the C-terminal tail domain is not well conserved in merlin and shows little association with F-actin (15, 27). Major binding targets of the FERM domain are adhesion molecules classified as type I membrane proteins. Biochemical studies have shown that the FERM domain binds the cytoplasmic regions of intercellular adhesion molecule-1 (ICAM-1), ICAM-2, and ICAM-3 of the immunoglobulin superfamily as well as CD44 and CD43/leukosialin/sialophorin (Fig. I-1-4) (13).

I-1-3. Aim of this study

The first crystal of the FERM domain bound to the target protein was obtained using the full-length adhesion molecule ICAM-2 cytoplasmic peptide comprising 28 residues (28). An x-ray structural study has shown how the radixin FERM domain binds the juxtamembrane region of the ICAM-2 cytoplasmic peptide. On the basis of crystal structure and mutation studies, the Motif-1 sequence motif, RXXTYXVXXA (where X represents any amino acid), is proposed as binding to the FERM domain. The ICAM-2 Motif-1 sequence forms a β strand (XXTY) that mediates anti-parallel β-β interactions with the FERM domain and a 3_{10}-helix (VXXA) that docks into a hydrophobic pocket. Motif-1 is found in other adhesion molecules of the immunoglobulin superfamily containing VCAM-1 and L1-CAM and proteoglycans such as syndecan and neurexin. All of these adhesion molecules

are shown to bind the radixin FERM domain. Recently, PSGL-1 (P-selectin glycoprotein ligand-1) has been shown to maintain a Motif-1-related sequence that binds the FERM domain (29). However, CD44 does not retains either Motif-1 or Motif-2, MDWXXXXX(L/I)FXX(L/F), which has recently been identified in the FERM-binding region of Na^+/H^+ exchanger regulatory factor-1 and -2 (NHERF-1 and -2) (30). Thus, the precise binding mode of CD44 to the FERM domain remains unclear.

Here, I carried out on physicochemical and hydrodynamic analyses of the CD44 cytoplasmic region and the crystal structure of the radixin FERM domain complexed with a CD44 juxtamembrane peptide. I show that the CD44 cytoplasmic region is present as a monomeric random coil in solution. In the complex crystal, the CD44 peptide binds subdomain C of the radixin FERM domain. The CD44 binding site overlaps with that of the Motif-1 binding site found in previous complexed structures (28, 29), whereas the binding mode of CD44 to the FERM domain is distinct from that of ICAM-2 and resembles that of the recently reported NEP (neutral endopeptidase 24.11) (31). These results, taken together with analyses of previous structures derived from the Hakoshima's laboratory, define a characteristic versatility of peptide recognition by the radixin FERM domain, which is distinct from the talin FERM domain (32) and PTB domains. Furthermore, in addressing how CD44 phosphorylation may interfere with binding to ERM proteins, I suggest a mechanism by which RIP-mediated cleavage of the CD44 cytoplasmic peptide facilitates nuclear translocation for transcriptional activation. Finally, I suggest a structural basis for Smad1 interactions with activated CD44 bound to ERM protein and linked to actin cytoskeletons.

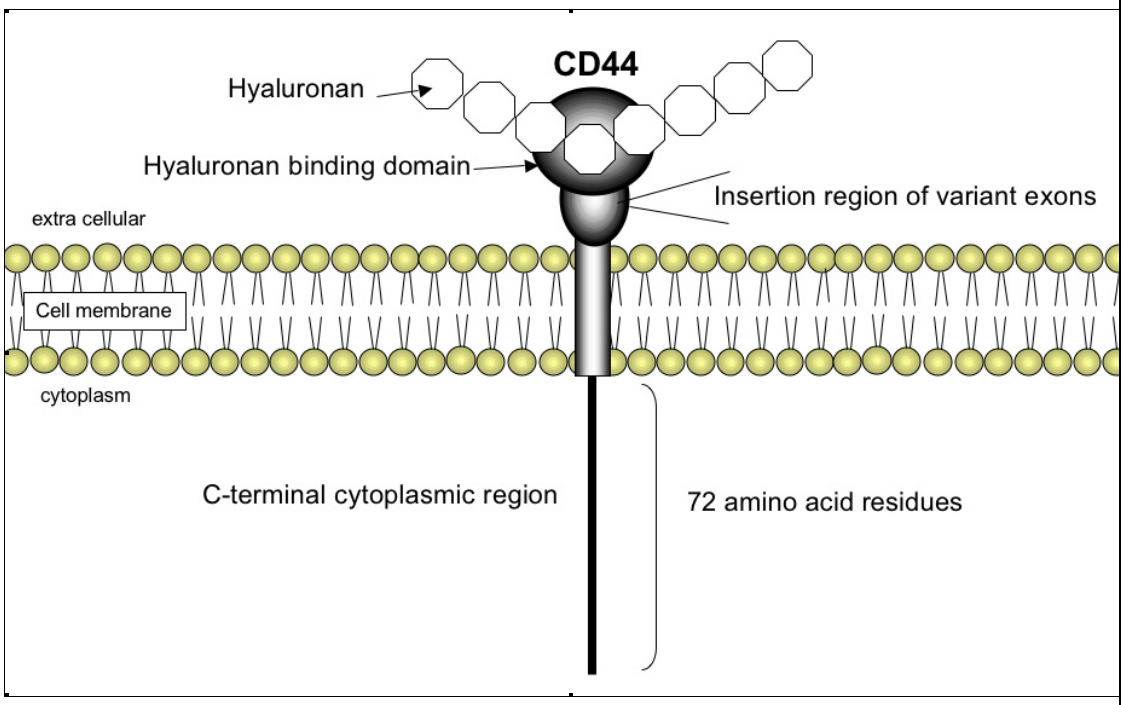

Fig.I-1-1 Domains of CD44

CD44 consists of 4 regions; a N-terminal hyaluronan binding domain, an insertion region of variant exon, a transmembrane helix and a C-terminal cytoplasmic region that comprises 72 amino acid residues. The cytoplasmic region associates with multiple proteins containing ERM proteins, ankyrin, and guanine nucleotide exchange factors of the Rho family, such as Tiam1 and 2 (T-lymphoma invasion and metastasis 1 and 2) (45–47).

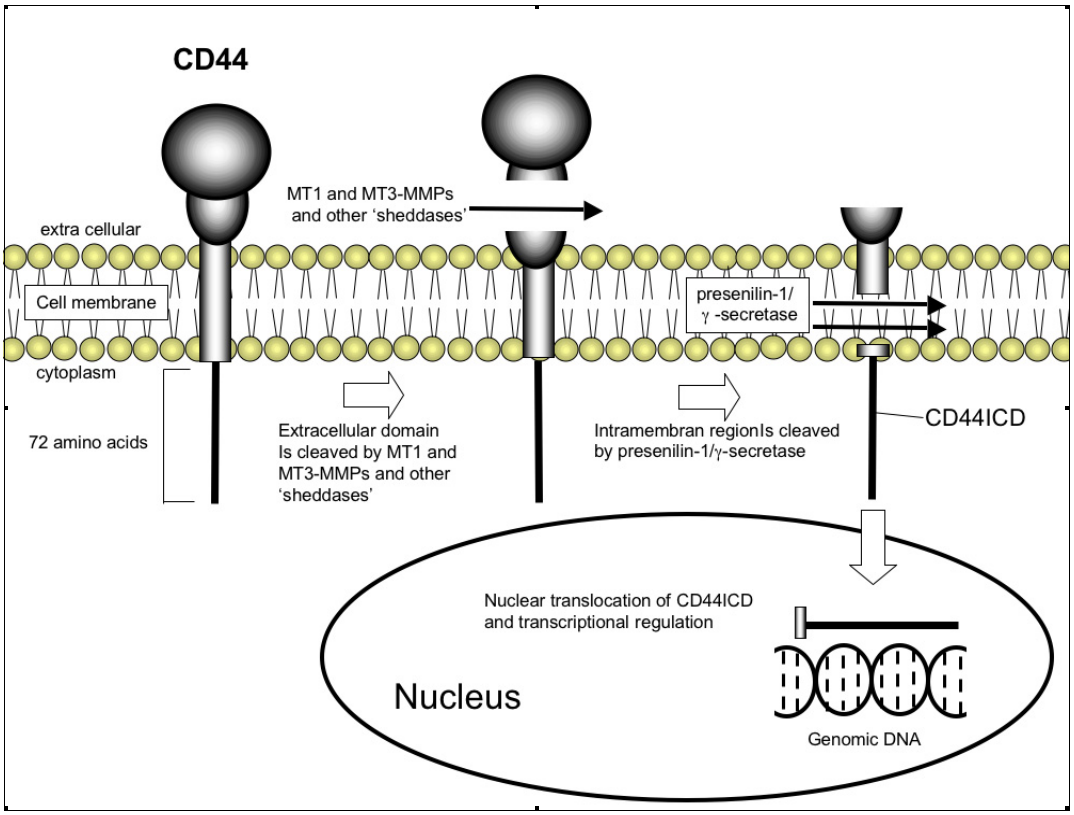

Fig. I-1-2 The proteolytic processing of CD44.

The extracellular region of CD44 is proteolytically cleaved by MT1- and MT3- MMPs in addition to other CD44 sheddases and then CD44 transmembrane helix cleaved by presenilin-1/γ−secretase. CD44 intercellular domain (CD44ICD) released from cell membrane translocates into the nucleus and stimulates transcription such as CD44 via direct interactions with the transcriptional machinery.

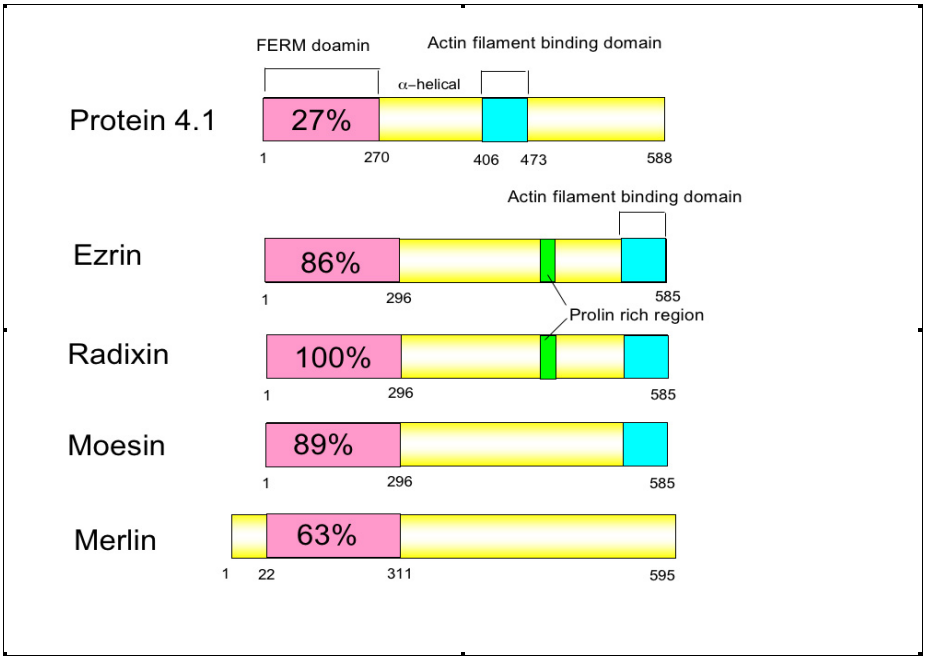

Fig. I-1-3 Protein 4.1, ERM proteins and merlin are closely related.

These proteins contain a FERM domain at the N-terminal region. Protein 4.1 shows poor sequence identity with the FERM domain of ERM proteins and merlin. ERM proteins have C-terminal actin binding region, whereas merlin does not. Therefore, merlin shows little association with F-actin. Ezrin and radixin have a proline rich region (green), function of which is unknown.

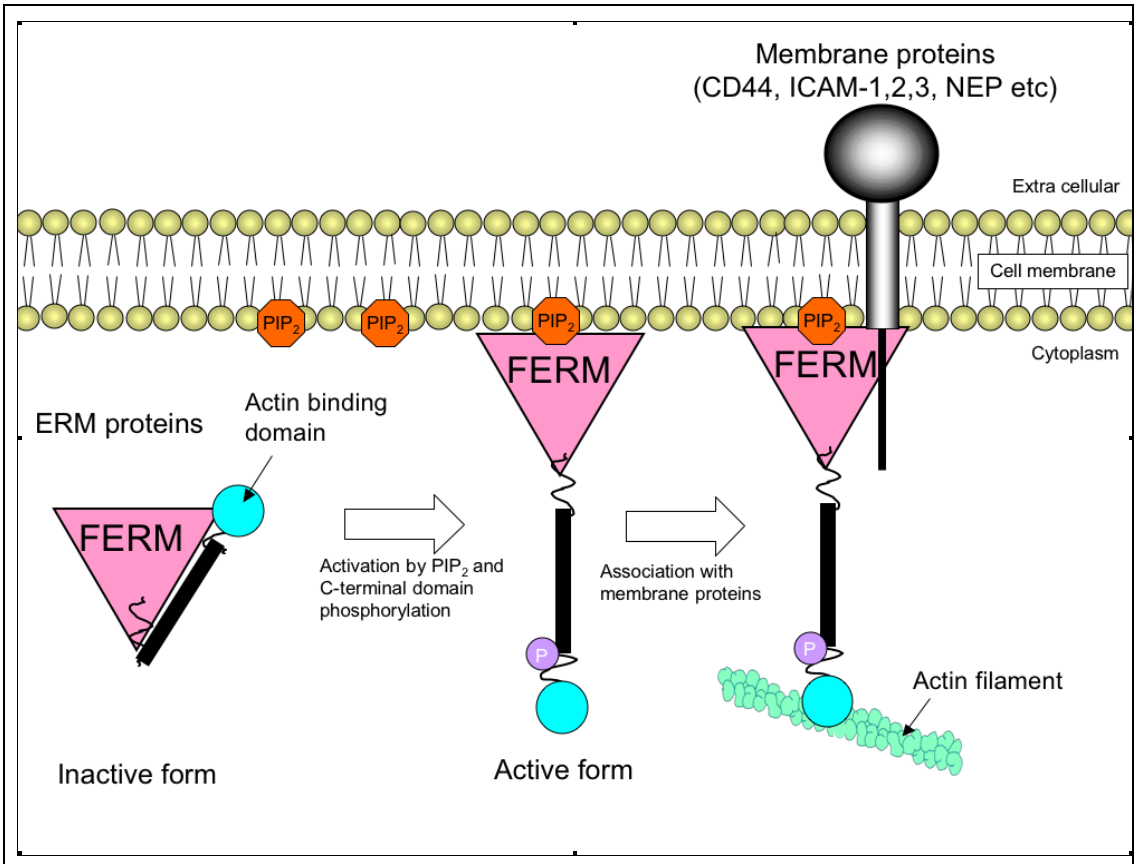

Fig.I-1-4 Membrane targeting and activation of ERM proteins.

In cytoplasm, ERM proteins are negatively regulated by intramolecular interaction between the FERM domain and the C-terminal domain (inactive form). Production of PIP_2 stimulates recruitment of ERM proteins to the plasmamembrane, wherei phosphorylation of the C-terminal conserved threonine occurs. These processes induce dissociation of the C-terminal domain from the FERM domain. Activated ERM proteins can participate in formation of the actin filament-plasma membrane linkage by direct interaction with membrane proteins such as CD44, ICAM-1,2,3, CD43 and NEP.

I-2. Materials and Methods

I-2-1. Expression and purification of CD44 cytoplasmic region

The region of cDNA coding for the cytoplasmic region of mouse CD44 (residues 292–363) was subcloned into pGEX6P-3 plasmid (GE Healthcare) using the *BamH* I and *Sma* I restriction enzyme sites. The CD44 cytoplasmic region was expressed in *Rosetta2(DE3)* cells (Novagen) as a fusion protein with glutathione S-transferase (GST). Cells were grown at 37 °C in Luria-Bertani (LB) medium containing 50 μg ml^{-1} ampicillin and 50 μg ml^{-1} chloramphenicol. When the OD_{660} of the cell culture reached 0.8, isopropyl β-D-thiogalactopyranoside (IPTG) was added to a concentration of 1 mM to induce expression of the CD44 gene. Cells were grown at 30 °C for an additional 5 hours following IPTG induction and then collected by centrifugation at 4000 rpm (Beckman J2-M1 JA10 rotor) for 15 min at 4 °C. Wet cells expressing CD44 peptide were suspended in 50 mM Tris buffer (pH 8.0) containing 500 mM NaCl, 1 mM dithiothreitol (DTT), 1 mM ethylenediamine tetraacetic acid (EDTA) and then disrupted by sonication at 4 °C. The soluble portion of the cell extract was then loaded onto a glutathione S-transferase affinity column comprising glutathione-Sepharose 4B resin (GSH resin) (GE Healthcare) and then washed copiously with 20 mM HEPES buffer (pH 7.3) containing 200mM NaCl, 1mM DTT, and 1mM EDTA. Bound glutathione S-transferase fusion protein was cleaved from the GSH resin using 5 units ml^{-1} thrombin (Sigma) for 8 hours or 2 units ml^{-1} HRV3C protease (Novagen) for 18 hours at 4 °C. The expected peptide of the construct begins after 5 extra residues (Gly-Pro-Leu-Gly-Ser) that are a part of the

HRV3C protease recognition sequence. The cleaved sample was collected and purified by chromatography using HiTrap SP (GE Healthcare) and HiPrep 26/10 desalting (GE Healthcare) with 10 mM HEPES buffer (pH 7.5) containing 50 mM NaCl and 0.5 mM DTT. The purified CD44 was concentrated using MicrosepTM centrifugal devices 1K (Pall Corp.). The sample was divided into 50 μl aliquots in 0.5 ml tubes (Eppendorf) and immediately frozen in liquid nitrogen. Frozen samples were stored at -80 °C until use.

I-2-2. Preparation of CD44 juxtamembrane peptide

The synthetic peptide corresponding to the juxtamembrane region (^{2}SRRRCGQKKKLVINGGNGTV^{21}) of the mouse CD44 cytoplasmic region was purchased from Toray Research Center (Tokyo Japan). This CD44 juxtamembrane peptide consists of 20 N-terminal residues encompassing the reported FERM domain binding region (13). The CD44 juxtamembrane peptide was dissolved at a concentration of 12 mM in 20 mM MES buffer (pH 6.8) containing 300 mM NaCl and 1 mM DTT, divided into 25 μl aliquots in 0.5 ml tubes (Eppendorf) and then stored at -80 °C until use.

I-2-3. Expression and purification of radixin FERM domain

The region of cDNA coding for the mouse radixin FERM domain (residues 1-310) was subcloned into pET49b(+) plasmid (Novagen) using the *Sma* I and *EcoR* I restriction-enzyme sites. FERM domain was expressed in *Rosetta2(DE3)pLysS* cells

(Novagen) as a fusion protein with GST. Cells were grown at 37 °C in LB medium containing 50 mg ml^{-1} kanamycin and 50 mg ml^{-1} chloramphenicol. When OD_{660} of the cell culture reached 0.6, IPTG was added to a concentration of 1 mM to induce expression of the FERM domain gene. Cells were grown for an additional 2 hours following IPTG induction and were then collected by centrifugation at 4000 rev min^{-1} (Beckman J2-M1 JA10 rotor) for 15 min at 4°C. Wet cells expressing FERM domain were suspended in 50 mM MES buffer (pH 6.8) containing 500 mM NaCl, 1 mM DTT and 1 mM EDTA and then disrupted by sonication at 4°C. The soluble portion of the cell extract was then loaded onto a GSH affinity column comprising GSH resin (GE Healthcare) and then washed copiously with 20 mM MES buffer (pH 6.8) containing 200mM NaCl, 1mM DTT, and 1mM EDTA. GSH resin-bound GST-fusion FERM domain was cleaved from the resin using 4 units ml^{-1} HRV3C protease (Novagen) for 18 hours at 4°C. The expected peptide of the construct begins after two extra residues (Gly-Pro) that are a part of the HRV3C protease recognition sequence. The cleaved sample was collected and purified by chromatography using HiTrap SP (GE Healthcare) and Superdex 200 gel-filtration column (GE Healthcare) with 20 mM MES buffer (pH 6.8) containing 300 mM NaCl and 1 mM DTT. Purified FERM domain was concentrated to 36 mg ml^{-1} using Amicon Ultra centrifugal filter devices (10 000 MWCO, Millipore). Concentrated FERM domain was divided into 20-50 μl aliquots in 0.5 ml tubes (Eppendorf) and immediately frozen in liquid nitrogen. The human merlin FERM domain was purified as described previously (41). Frozen samples were stored at -80°C until use.

The identity of the purified protein was confirmed using matrix assisted laser desorption/ionization time-of-flight mass spectroscopy (MALDI TOF MS;

PerSeptive Inc.) and N-terminal sequence analysis (M492; Applied Biosystems).

I-2-4. Crystallization of radixin FERM domain and CD44 juxtamembrane peptide

The purified radixin FERM domain and the synthesized CD44 juxtamembrane peptide were mixed in a 1:5 molar ratio [0.3 mM FERM and 1.5 mM CD44 peptide] with 20 mM MES buffer (pH 6.8) containing 300 mM NaCl and 1 mM DTT (protein solution 1). Initial screening of the crystallization conditions was carried out with the sitting-drop vapour diffusion method at 4°C using a HYDRA II (Scrum) and commercial crystallization screening kits (Qiagen; PEGs I, PEGs II, JCSG, pH Clear, MB Class, MB Class II, Classics, Classics Lite, ProComplex and the PACT suite). FERM-CD44 peptide complex crystals were obtained within 3 days by mixing 0.2 μl protein solution 1 with 0.2 μl PACT suite reservoir solution No. 88 [0.1 M bis-Tris buffer pH 8.5 containing 20% polyethylene glycol 3350 (PEG 3350) and 0.2 M potassium thiocyanate]. Crystallization conditions were then refined by changing the pH (between 8.0 and 8.7 in increments of 0.1) and the PEG 3350 concentration (15-25% in 5% increments). The crystals obtained from the initial screening appeared to be clustered and stacked. A microseeding method was then employed in an effort to obtain single crystals suitable for X-ray diffraction. Crystals for microseeding were obtained using the hanging-drop vapour-diffusion method at 4 °C. FERM and CD44 juxtamembrane peptide were mixed in a 1:20 molar ratio [0.3 mM FERM and 6 mM CD44 juxtamembrane peptide] with stock buffer (protein solution 2). The drop was comprised of 1 μl protein solution 2 and 1 μl reservoir

solution containing 0.1 M Tris pH 8.6, 25% PEG 3350 and 0.2 M potassium thiocyanate. Clustered crystals were obtained after 3 days. These crystals were crushed in 10 μl 0.1 M Tris pH 8.6 containing 15% PEG 3350 and 0.2 M potassium thiocyanate (seed solution) using a glass homogenizer (Radnoti). The solution was then diluted 5000-fold with the same buffer. Microseeding was carried out by the sitting-drop vapour diffusion method at 4°C. A 0.5 μl aliquot of the diluted seed solution was mixed with 2.5 μl protein solution 2 and 2 μl reservoir solution. Rod-like crystals of the FERM-CD44 complex were obtained within 10 days (Fig. I-2-1).

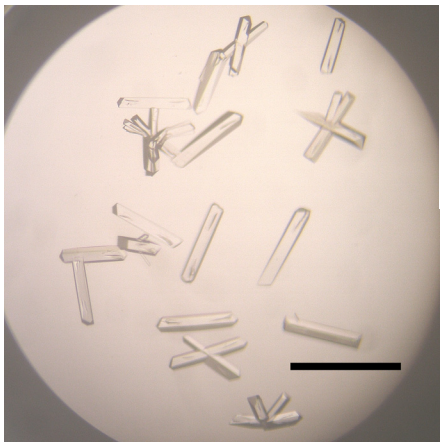

Fig. I-2-1 Rod-shaped crystals of the complex formed by FERM with CD44 obtained by microseeding. The scale bar indicates 0.5 mm.

I-2-5. X-ray data collection of the FERM-CD44 complex

Crystals for diffraction studies were transferred stepwise into a cryoprotective solution consisting of 0.05 M Tris buffer pH 8.6 containing 0.15 M NaCl, 0.1 M potassium thiocyanate, 20% PEG 3350 and 20% PEG 200 for flash-cooling. X-ray diffraction data were collected from the FERM-CD44 peptide complex crystal using a Rigaku MSC Jupiter 210 detector installed on beamline BL38B1 at SPring-8, (Harima, Japan). The crystal data and the intensity data statistics are summarized in Table I-1. Diffracted x-ray intensities were processed using the HKL-2000 program suite (35).

I-2-6. Structural determination and refinement of the FERM-CD44 Complex

Phases were determined by molecular replacement using the program PHASER (36) with the free form structure of the FERM domain as a search model (37). The procedure gave a clear solution corresponding to one FERM molecule in the asymmetric unit of the crystal. The calculated molecular replacement maps showed definite residual electron densities for the CD44 peptide at the groove between strand β5C and helix α1C of subdomain C of the FERM domain in both 2*Fo* - *Fc* and *Fo* - *Fc* maps. CD44 peptide residues were modeled manually using O (38). The complex structure was refined by simulated annealing, followed by restrained individual B-factor refinement performed using the program CNS (39). The refinement statistics are summarized in Table 1. The stereochemical quality of the model was assessed using the program PROCHECK. In the Ramachandran plot, 89.8

and 9.9% of residues were located within the most favored and additional allowed regions, respectively. One exceptional outlier was flagged in the plot, that of Asp252 located within a type II reverse turn between strands β5C and β6C. This outlier repeatedly appeared in the FERM domain structures of radixin (28, 30, 37), moesin (40), and merlin (41). The structure was also checked with MolProbity (42). In the Ramachandran plot, 96.3, 3.3, and 0.3% (Lys296 but not Asp252) of the residues fell in favored, allowed, and outlier regions. Thus, judgment of outliers in the structure is subtle. Molecular illustrations were prepared using the program PyMOL (DeLano Scientific). Superposition of the FERM domains and peptides were performed using the program Lsqkab (43).

I-2-7. Analytical ultracentrifugation of CD44 cytoplasmic region

Sedimentation velocity ultracentrifugation experiments were performed at 10 °C using a Beckman Coulter Optima XLA analytical ultracentrifuge equipped with an An-60 Ti rotor and double sector centerpieces. Purified samples of the CD44 cytoplasmic region were dissolved in 5 mM Tris buffer (pH 7.8) containing 50 mM NaCl and 2 mM DTT (TSD buffer) at a sample concentration of 0.5 mg ml^{-1} and then centrifuged at 42,000 rpm. Radial absorbance scans were measured every 15 min at a wavelength of 230 nm. The resultant data were analyzed using the programs Sedfit and Sednterp. To glean further insight into the CD44 conformation in the FERM-bound state, similar experiments were performed for the FERM domain in the free and the CD44 bound forms in 5 mM Tris buffer (pH 7.4) containing 150 mM NaCl at 20 °C.

Sedimentation equilibrium ultracentrifugation experiments were performed at 10 °C using the same ultracentrifuge and rotor as described above. Six-sector centerpieces were used. The CD44 cytoplasmic region was dissolved in TSD buffer at sample concentrations of 0.0625, 0.125, and 0.25 mg ml^{-1} and then centrifuged at 32,000, 38,000, 40,000, and 48,000 rpm. Radial absorbance scans were measured at 230 nm after 22 hours, at which time equilibrium had been achieved. The resultant data were analyzed using XLA/XL-I data analysis software.

I-2-8. Circular dichroism (CD) spectroscopy of CD44 cytoplasmic region

CD spectra of the purified CD44 cytoplasmic region were recorded at 4 °C using a Jasco J720W spectropolarimeter. The CD44 cytoplasmic region was dissolved in 5 mM Tris buffer (pH 8.0) containing 50 mM NaCl, 0.7 mM EDTA, and 0.5 mM 2-mercaptoethanol or containing 150 mM NaCl, 0.7 mM EDTA, and 0.5 mM 2-mercaptoethanol. The CD44 cytoplasmic region and the FERM domain were mixed at a 1:1 molar ratio (13 μM:13 μM) and dissolved in 5mM Tris buffer (pH 8.0) containing 150 mM NaCl, 0.7 mM EDTA, and 0.5 mM 2-mercaptoethanol. Secondary structure estimations were calculated using the Jasco secondary structure estimation software.

I-2-9. Pull-down assay of the radixin FERM domain with wild type, S2D, and S2p of CD44 Peptides

N-terminal biotinylated CD44 cytoplasmic peptides were purchased from

Toray Research Center (Tokyo, Japan) for the *in vitro* binding assay. The wild-type CD44 peptide (^{2}SRRRCGQKKKLVINGGNGTV^{21}) is the same as that used in the x-ray structural work. The S2p peptide (^{2}*Sp*RRRCGQKKKLVINGGNGTV^{21}) contains phosphoserine at position 2, and the S2D mutant peptide (^{2}*D*RRRCGQKKKLVINGGNGTV^{21}) contains a negatively charged aspartic acid that mimics the phosphorylated state of Ser2. Pull-down assays were performed using Streptavidin Sepharose high performance resin (GE Healthcare). For each reaction, 25 μl of the resin was mixed with 25 pmol of each N-terminal biotinylated peptide and suspended in 1 ml of 10 m*M* HEPES buffer (pH 7.4) containing 70 m*M* KCl and 1 m*M* DTT (pull-down buffer) in a 1.5-ml tube (Eppendorf). Resin free from bound peptide was used as the control. The resin was harvested as a pellet by centrifugation (2000 *g* for 1 min). After removing the supernatant, the resin was suspended in 1 ml of pull-down buffer again, and this wash was repeated two times. 25 μl of 100 μ*M* FERM domain dissolved in pull-down buffer was added to the resin. The resin was incubated for 2 hours at room temperature with occasional mixing and then washed two times with pull-down buffer by centrifugation. To elute the streptavidin-bound peptide and its associated FERM domain, 25 μl of SDS-sample buffer was added to recovered resin, and then each sample was incubated for 5 min at 96 °C. The amount of streptavidin in each eluate was determined by SDS-PAGE, and eluted proteins were visualized using SimplyBlueTM SafeStain (Invitrogen). An appropriate amount of each eluate containing the same amount of streptavidin was then subjected to SDS-PAGE. The amount of bound FERM domain was determined by densitometric scanning using the software Image J 1.36b. The relative amount of the FERM domain bound per streptavidin was calculated, and the amount of FERM domain bound to the

control resin was subtracted from each eluate. This pull-down assay was performed three times, and the average amount of FERM domain binding to each peptide was estimated.

I-2-10. Binding assay using BIAcore

The binding affinity for the 23-residue CD44 peptide was examined by using equilibrium surface plasmon resonance measurements, which were carried out on a Biacore Biosensor instrument (Biacore 3000; GE Healthcare), as previously described (30). The biotinylated peptide of the juxtamembrane region was purchased from Sawady Technology (Tokyo, Japan). The peptide was coupled via the N-terminal biotin moiety to a streptavidin-coated sensor chip (sensor chip SA Biacore AB). The purified FERM domain (5–1280 nM) was injected into both peptide-linked and nonlinked sensor chips for correction of background signals. All binding experiments were per-formed at 25 °C with a flow rate of 20 μl/min in buffer consisting of 10mM HEPES (pH 7.4), 150mM NaCl, 1mM EDTA, 1mM DTT, and 0.005% surfactant P20. The kinetic parameters were evaluated by using the BIA evaluation software (GE Healthcare). The K_D values were obtained by averaging of at least three independent measurements. The obtained K_D values for FERM binding to the 23-residue CD44 peptide are 110.9 nM (melin FERM domain) and 120.9 nM (radixin FERM doman).

Table 1-1. Crystallographic data for the radixin FERM domain-CD44 complex

X-ray data	
Space group	$P2_12_12_1$
Cell parameters, (Å)	a = 62.70, b = 66.18, c = 86.22
Wavelength (Å)	1.0000
Resolution (Å)[a]	20-2.10 (2.17-2.10)
Mosaicity	0.5-0.8
Reflections, total/unique	156,148 / 21,492
Completeness (%)	100.0 (100.0)
$< I/\sigma_I >$	12.2 (4.9)
R_{merge} (%)	5.0 (36.1)
Refinement	
Number of residues included	
FERM (residues 1-310)	295 (residues 3-297)
CD44 (residues 2-21)	9 (residues 8-16)
Water	171
Number of atoms	2,714
R_{work} / R_{free} (%)[b]	23.1 / 25.6
Average B-factor (Å^2)	
FERM	37.0
CD44	60.8
Water	42.6
R.m.s. bond length (Å), angles (º)	0.006, 1.2

[a] Numbers in parentheses refer to statistics for the outer resolution shell.

[b] $R_{work} = \Sigma \mid \mid F_{obs} \mid - \mid F_{calc} \mid \mid / \Sigma \mid F_{obs} \mid$. R_{free} is the same as R_{work} except for a 5% subset of all reflections that were never used in the crystallographic refinement.

I-3. Results

I-3-1. Conformational properties of the CD44 cytoplasmic region in solution

The structural features of the CD44 cytoplasmic region, comprising 72 amino acid residues, are largely unknown. One intriguing question relates to whether this longer cytoplasmic region forms a stable compact domain that possesses the ability of self-association to form dimeric or oligomeric structures. In an effort to address these uncertainties, analytical ultracentrifugation methods were employed to investigate the assembly state of the whole cytoplasmic region and to determine the approximate shape of the molecule/assembly in solution.

Sedimentation equilibrium analyses resulted in an excellent fit of the observed absorbance data with the calculated curve based on an ideal single-species model (Fig. I-3-1). The obtained molecular mass of 8.8 kDa is close to the theoretical value (8.382 kDa) and suggests that the CD44 peptide adopts a monomeric form in solution.

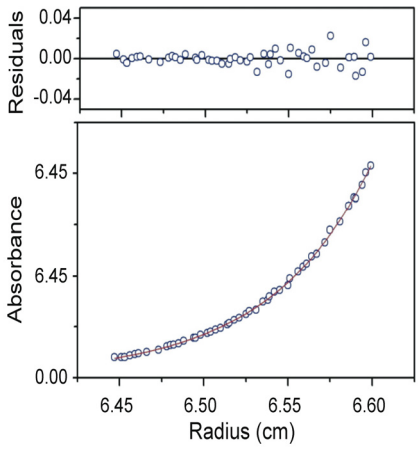

Fig. I-3-1 Sedimentation equilibrium data with a fitted curve for the 0.25mg ml^{-1} CD44 cytoplasmic region solution at 38,000 rpm. The *upper panel* shows residuals representing the difference between the calculated fit and the experimental data using XLA/XL-I data analysis software. The molecular mass of the CD44 cytoplasmic region was estimated to be 8.8 kDa. This result shows that the CD44 cytoplasmic region adopts a monomeric form in the solution state

Sedimentation velocity measurements showed the presence of a single boundary, which suggests monodispersity of the sample containing the molecular species with a sedimentation coefficient of 0.73 S and an estimated molecular mass of 10.4 kDa (Fig. I-3-2), which is similar to that of the sedimentation equilibrium experiments. Thus, it was demonstrated that the CD44 peptide adopts a monomeric form. Interestingly, the CD44 peptide adopts an elongated shape, as estimated from the obtained translational frictional ratio (f/f_0) of 1.89, which suggests a major/minor axial ratio (a/b) of 16.0. Supposing a diameter of 1.5 nm for a peptide chain in a random coiled state, the obtained a/b value suggests that the cytoplasmic peptide extends by ~24 nm out from the inner cell membrane toward the cytoplasmic region or otherwise parallel to the membrane. The juxtamembrane region that is rich in basic residues might run parallel to the membrane and interact with the negatively charged inner membrane surfaces. The rest of the peptide residues, however, may not be parallel to the membrane because of many negatively charged residues; it contains 11 acidic but only 6 basic residues.

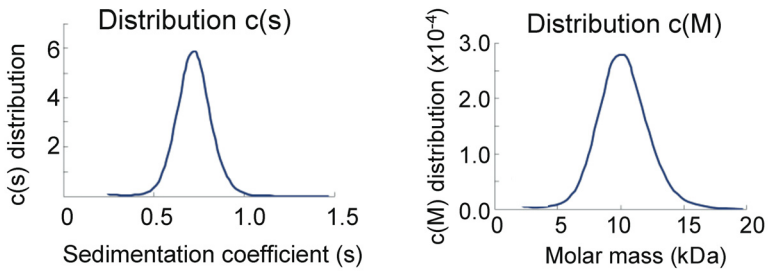

Fig. I-3-2 The distribution of sedimentation coefficients obtained from sedimentation velocity analysis of the CD44 cytoplasmic region. The single peak is found at 0.73 S (left panel). The distribution of apparent molecular mass obtained from sedimentation velocity analysis of the CD44 cytoplasmic region. The single peak is found at 10.4 kDa (light panel).

Further insight into the secondary structure was gleaned by examination of the CD spectra of the CD44 cytoplasmic region. The spectra obtained clearly suggested the absence of typical secondary structures, such as the α-helix and β-sheet, at a sample concentration of 0.1 mg ml^{-1} (13 μM). Titration of the FERM domain induced no significant spectral changes, suggesting that the CD44 cytoplasmic region is present largely as a random coil without global secondary structural changes when bound to the FERM domain (Fig. I-3-3).

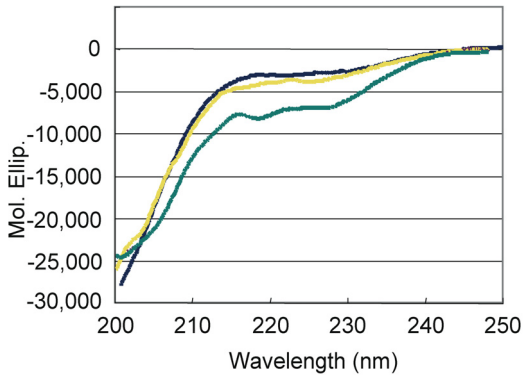

Fig. I-3-3 CD spectra of the 72-residue CD44 cytoplasmic region. Spectra of the CD44 peptide at 50mM NaCl (*blue*) and 150 mM (*yellow*) are shown with a difference spectrum between the FERM domain and the 1:1 complex of the radixin FERM domain and CD44 (*cyan*).

Thus, the interaction between radixin and CD44 could be more appropriately described as a protein-peptide interaction rather than a protein-protein interaction. To verify that notion, I again performed analytical ultracentrifugation with the free and CD44-bound FERM domain. Sedimentation velocity measurements showed estimated molecular masses indicating monomers (Fig. I-3-4). Quantitative analysis revealed an increase of the sedimentation coefficient (2.82 S) by complex formation and suggested an *a*/*b* ratio of 8.2 (the f/f_0 ratio of 1.65). This large ellipticity implies the lack of structure of most of the CD44 peptide in the complex, which is consistent with the lack of changes in CD spectra in the titration experiment.

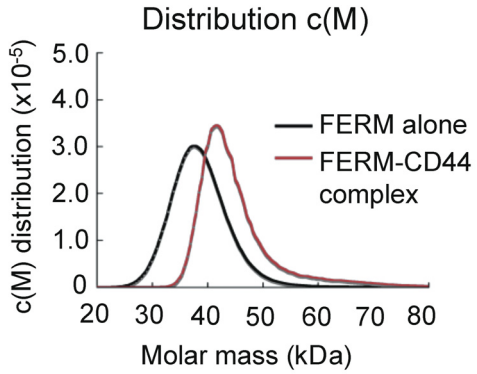

Fig. I-3-4 Distribution of apparent molecular mass obtained from sedimentation velocity analysis of the FERM domain in the free and the CD44 cytoplasmic region bound forms. Estimated molecular masses are 38.7 kDa (free form) and 44.1 kDa (CD44-bound form), suggesting monomers.

I-3-2. Crystal structure determination

I set out to determine the crystal structure of the complex between the mouse radixin FERM domain (residues 1–310) and the CD44 peptide. As expected from the flexible nature of the CD44 cytoplasmic tail in solution, crystallization trials carried out using the 72-residue CD44 cytoplasmic region were unsuccessful. A previous biochemical study has shown that moesin binds 19- and 32-residue juxtamembrane regions of CD44 cytoplasmic tails, whereas deletion of the 19 juxtamembrane residues from the cytoplasmic region almost completely abolished binding (13). The quantitative binding assay using surface plasmon resonance measurements showed that both the marlin and radixin FERM domain bind a CD44 peptide comprising 23 juxtamembrane residues with dissociation constant (K_D) values of 110.9 and 120.9 n*M*, respectively (Fig. I-3-5).

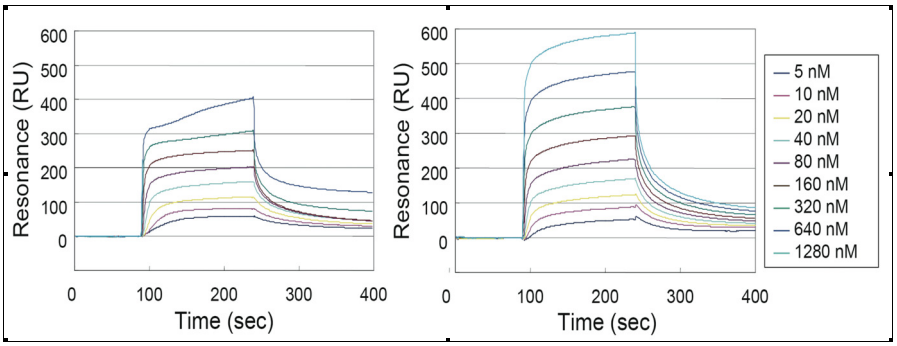

Fig. I-3-5 The sensorgrams for each concentration of the merlin (*left*) or radixin (*right*) FERM domain. The signals from the control surface were subtracted. The dissociation constant (K_D) values are 110.9 nM (merlin) and 120.9 nM (radixin), respectively.

These values are consistent with a reported quantitative binding assay involving surface plasmon resonance measurements using a longer (37-residue) CD44 peptide (28). Accordingly, the crystallization trials that followed made use of shorter CD44 juxtamembrane peptides of different lengths. I found that a FERM-CD44 complex crystal suitable for structure determination was obtained using the 20-residue juxtamembrane peptide of mouse CD44 (residues 293–312; sequence ^{2}SRRRCGQKKKLVINGGNGTV^{21}). The peptide residues encompass the previously reported 19-residue region that was shown to directly interact with moesin (13). For convenience, the peptide residues are numbered from 2 to 21, corresponding to the 72 cytoplasmic residues. The crystals contained one FERM-CD44 complex in the asymmetric unit. The structure of the FERM-CD44 complex was determined by molecular replacement and subsequently refined to 2.1 Å resolution with an *R*-value of 23.1% (and a free *R*-value of 25.6%). The crystallographic statistics are summarized in Table 1. On the current electron density map, the CD44 peptide model contains 9 residues (positions 8–16) of 20. No models were built for two N-terminal

and 13 C-terminal residues of the FERM domain, which were not observed in the electron density map.

I-3-3. Structure of the radixin FERM domain in the complex

The radixin FERM domain bound to CD44 comprises three subdomains: subdomain A (N-terminal residues 3–82; *green*) having a typical ubiquitin fold, subdomain B (residues 95–195; *red*) folded into an α-helix bundle, and subdomain C (residues 204–297; *yellow*) folded into a standard seven-stranded β-sandwich with a long capping α-helix (Fig. I-3-6 *A*). These structural characteristics are identical to previously reported structures of the radixin FERM domain (28, 29, 31, 37). The overall root mean square deviation between the FERM domain bound to the CD44 peptide and the free radixin FERM domain is 0.76 Å for 292 Cα carbon atoms (residues 5–296), suggesting no significant structural changes in the global structure.

I-3-4. CD44 recognition by the radixin FERM domain

The CD44 peptide binds subdomain C, whose fold could be classified as a phosphotyrosine binding (PTB) domain (37) (Fig. I-3-6 *A*). The binding region of CD44 encompasses residues 8–16, which contains one of the basic clusters, KKK, followed by a nonpolar region (Fig. I-3-6 *B*). Along the hydrophobic shallow groove formed by helix α1C and strand β5C from subdomain C, the peptide forms a short β strand structure (residues 9–12; Lys-Lys-Lys-Leu), which augments the β sheet formed by strands β5C-β7C from subdomain C. The groove creates side chain

binding sites, *S1–S4*, that interact with side chains of the CD44 peptide (Fig.I-3-6 *B*). The CD44 β strand forms five regular main chain–main chain hydrogen bonds with strand β5C (Fig.I-3-7, *A* and *B*). A short loop structure (residues 13–16; Val-Ile-Asn-Gly) follows the β strand and docks into a pocket *P1* connected to the hydrophobic groove. Two hydrophobic residues of the CD44 peptide, Leu12 and Ile14, position the aliphatic side chains into the deep hydrophobic *S4* site and *P1* pocket, respectively (Fig. I-3-6 *B*). The main chain of Ile14 is hydrogen-bonded to His288 from helix α1C. Importantly, the CD44 loop residues form three main chain-main chain hydrogen bonds with the end of strand β5C and the following loop β4C-β5C residues (Fig. I-3-7, *A* and *B*). In addition to the main chain-main chain interactions, the side chain of CD44 Asn15 forms a hydrogen bond with the main-chain carbonyl group of Trp242 from loop β4C-β5C and probably with those of other loop residues (Ile245 and Ser243). The side chains of Gln8 and three lysines (Lys9, Lys10, and Lys11) of the β strand appear as partially disordered in the electron density map (Fig. I-3-6 *C*) and are obviously flexible, exposing the side chain end groups toward the solvent region in the absence of direct contacts with the FERM domain. Three lysines, however, have the aliphatic bases of their side chains positioned on the *S1–S3* sites (Fig. I-3-6 *B*). Notably, the positively charged terminal groups are oriented toward the proposed plasma membrane (Fig. I-3-8). The radixin residues that participate in interactions with the CD44 peptide are well conserved in other ERM members, such as ezrin and moesin, and merlin, suggesting that the observed binding mode in the structure could also be expected in the case of interactions with other ERM proteins as well as merlin (Fig. I-3-7 *C*).

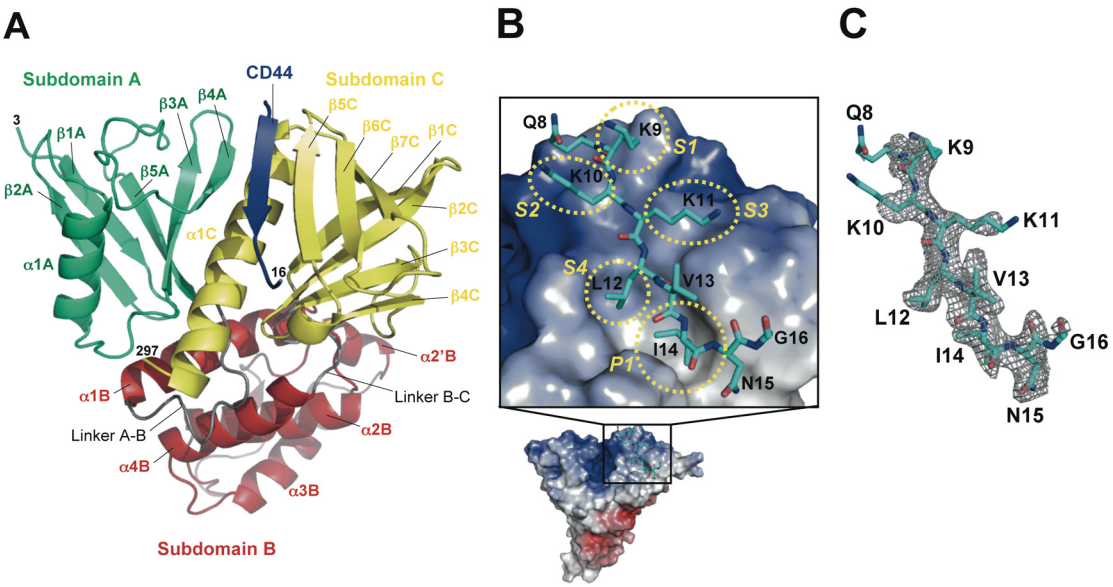

.

Fig. I-3-6 Crystal structure of the FERM-CD44 complex

A, *ribbon representations* of the radixin FERM domain complexed with the CD44 cytoplasmic peptide (*blue*). The radixin FERM domain comprises three subdomains: A (residues 3–82 in *green*), B (residues 96–195 in *red*), and C (residues 204–297 in *yellow*). Linkers A-B (residues 83–95) and B-C (residues 196–203) are colored *gray*.

B, surface electrostatic potentials of the FERM domain and a close-up view of the CD44 cytoplasmic peptide docked into the groove formed between helix α1C and strand β5C of subdomain C. The peptide is shown as a *stick model* (labeled with *one-letter codes*), and the four side chain-binding sites (*S1-S4*) for the bound β strand of CD44 and the deep hydrophobic pocket (*P1*) are *labeled* and indicated with *yellow dashed circles*. Site *S4* adjoins pocket *P1*.

C, a *stick model* of the CD44 cytoplasmic peptide is shown in the omit electron density map for the CD44 cytoplasmic peptide at the contour level of 1σ.

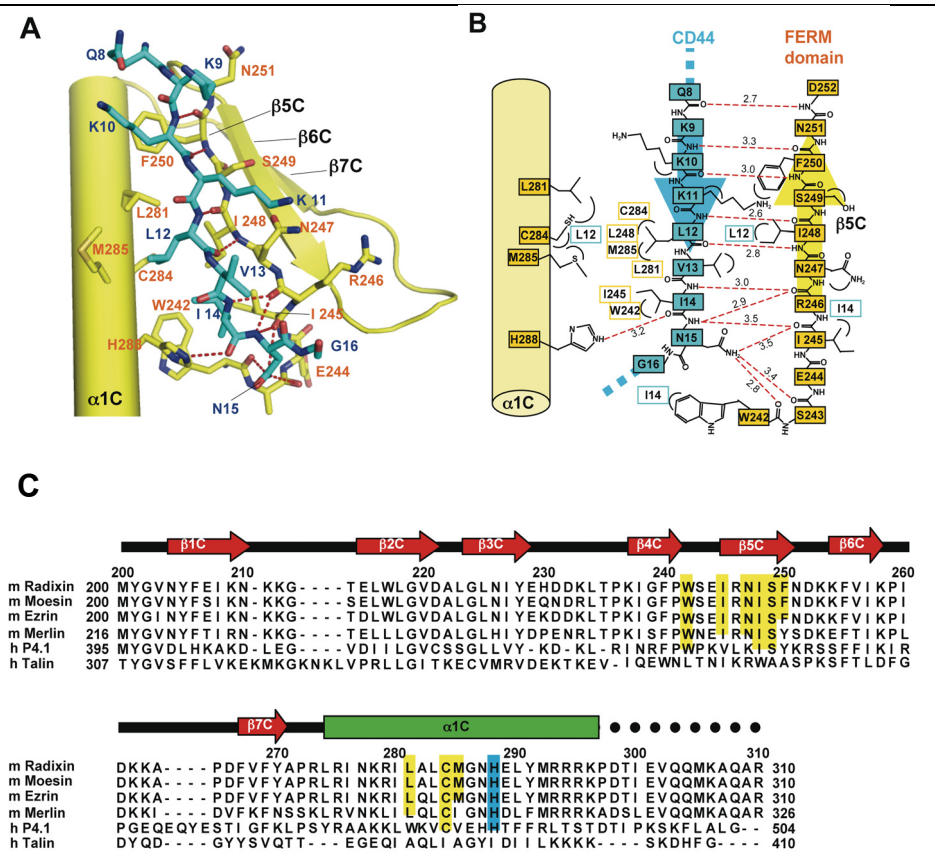

Fig. I-3-7. CD44 binding to subdomainC of the FERM domain and sequence alignment of subdomainC of ERM and related proteins.

A, the CD44 cytoplasmic peptide (*blue stick model*) binds the groove between helix α1C (*yellow cylinder*) and strand β5C (*yellow stick*) of subdomain C of the FERM domain. Hydrogen bonds are shown as *red dashed lines*.

B, schematic representation of the interactions between the CD44 cytoplasmic peptide (*blue*) and subdomain C (*yellow*). The nonpolar contacts involving side chains are shown with contacted residues. Two hydrogen bonds formed by the main chain carbonyl group of FERM Ile245 with the main and side chains of CD44 Asn15 are relatively long (3.45 Å).

C, sequence alignment of subdomain C of mouse (*m*) radixin, ezrin, moesin, human band 4.1 protein (*h P 4.1*), and talin (*h Talin*). The secondary structure of the radixin FERM subdomain C is shown at the *top*. *Green rectangle*, α-helix; *red arrows*, β-strands. Residues that participate in nonpolar and polar interactions with the CD44 peptide are *highlighted* in *yellow* and *cyan*, respectively.

I-3-5. Comparison with the FERM-ICAM-2 complex

The CD44 binding site on subdomain C in the complex overlaps with that of the ICAM-2 peptide found in this FERM-ICAM-2 complex (28); both the CD44 and ICAM-2 peptides bind the groove between helix α1C and strand β5C of subdomain C and involve antiparallel β-β interactions with strand β5C (Fig. I-3-8). This similarity was unexpected given the lack of sequence homology between the two peptides; the juxtamembrane region of CD44 contains two clusters of basic residues followed by a nonpolar region and a glycine-rich stretch, whereas that of ICAM-2 contains a Motif-1 nonpolar region that is sandwiched between two basic regions (Fig. I-3-9). Structure based sequence alignment suggests that the QKKKLVINGG sequence of CD44 corresponds to the Motif-1 sequence of ICAM-2. With this alignment, CD44 replaces the Motif-1 RXXTY and XVXXA sequence stretches with QKKKL and XINGG sequences, respectively. Structural alignment revealed that conserved CD44 Ile14 corresponds to ICAM-2 Val12, and these 2 residues dock into the same *P1* pocket and are completely overlapped (Fig. I-3-10 *A*). Contrary to this excellent overlap, the side chain of CD44 Leu12 is shifted from that of ICAM-2 Tyr10, although both dock into the *S4* site. This is a consequence of the site not being large enough to accommodate the large tyrosine side chain of ICAM-2. Therefore, ICAM-2 orients the side chain of Tyr10 toward His288 of the FERM domains and forms a hydrogen bond (Fig. I-3-10 *C*). The VXXA stretch of the ICAM-2 peptide forms a 3_{10} helix, whereas the CD44 peptide fails to form a 3_{10} helix, probably due to the glycine-rich sequence that displays structural flexibility. CD44 lacks an Ala residue that is essential for docking the 3_{10} helix into the *P1* pocket, which contributes toward

stabilization of the helix. ICAM-2 possesses Leu13 instead of CD44 Asn15, which forms multiple hydrogen bonds to the main chains of loop β4C-β5C as described. In the FERM-ICAM-2 complex, ICAM-2 Leu13 is a component of the 3_{10} helix and projects the side chain from the pocket toward the side chain of Ile260 from loop β6C-β7C of the FERM domain (Fig. I-3-10 *C*). The ICAM-2 3_{10} helix also enables Trp16 to form a water-mediated hydrogen bond to His288. The large aromatic ring of Trp16 is located at the side of the *P1* pocket and replaces Asn15 of CD44.

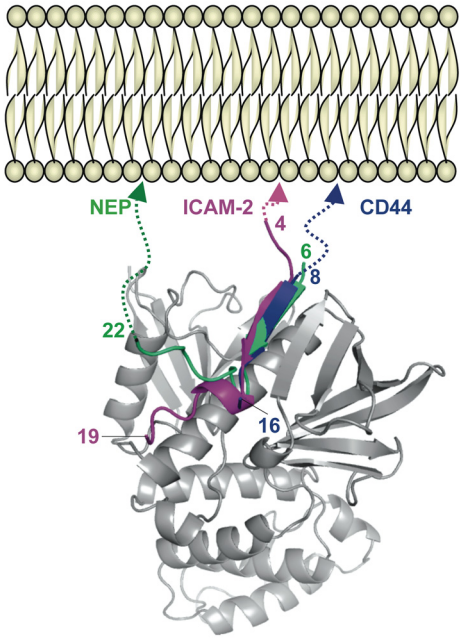

Fig.I-3-8. Comparison of ICAM-2, NEP, and CD44 peptides bound to the FERM domain. Shown is superposition of ICAM-2 (*magenta*) from the FERM-ICAM-2 complex (28) and NEP (*green*) from the FERM-NEP complex (31) on the FERM-CD44 complex. The N-terminal extensions of ICAM-2 and CD44 or the C terminus of NEP that would be linked to the transmembrane helix in the plasmamembrane are indicated with *dotted lines*.

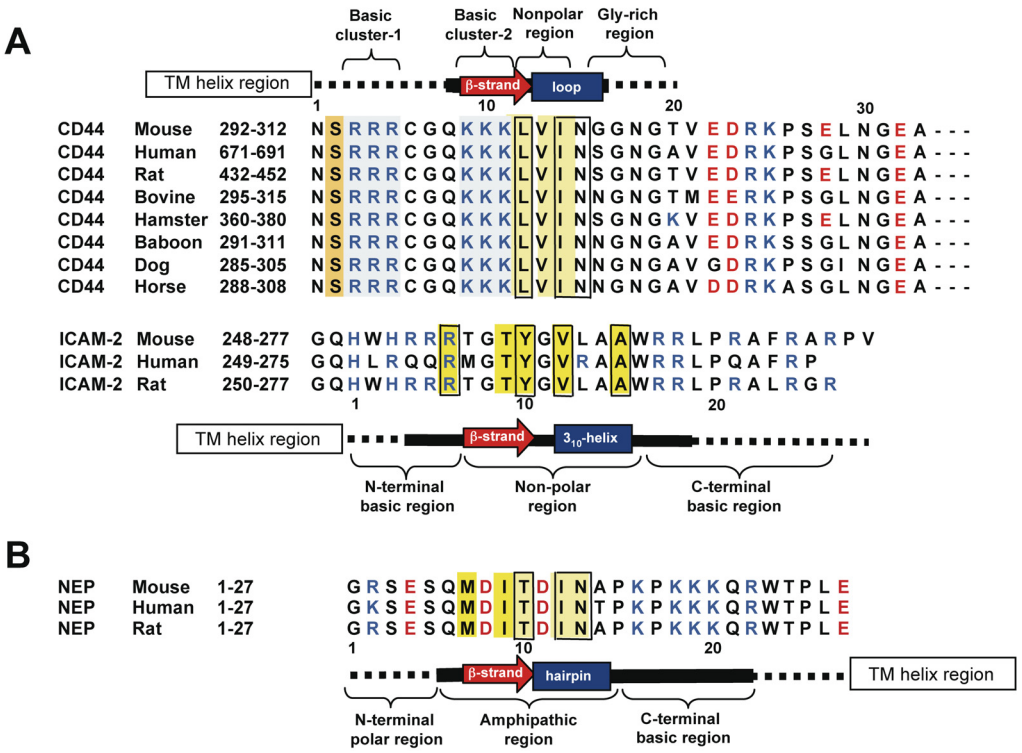

Fig. I-3-9 Comparison of FERM-binding peptide sequences.

A, alignment of the juxtamembrane regions of CD44 cytoplasmic tails is compared with that of ICAM-2. The secondary structures found in the FERM-CD44 complexed structure are shown at the *top* with those found in the FERM-ICAM-2 complex (28). The *solid boldface lines* indicate peptide residues defined in the maps, and the *dotted lines* indicate residues that were not defined in the maps. Basic and acidic residues are shown in *blue* and *red*, respectively, and key residues for binding are marked with *boxes* and *highlighted* in *yellow*. Two conserved basic clusters of CD44 are *highlighted* in *blue*.

B, alignment of the juxtamembrane regions of NEP cytoplasmic regions is shown together with the secondary structures found in the FERM-NEP complex (31).

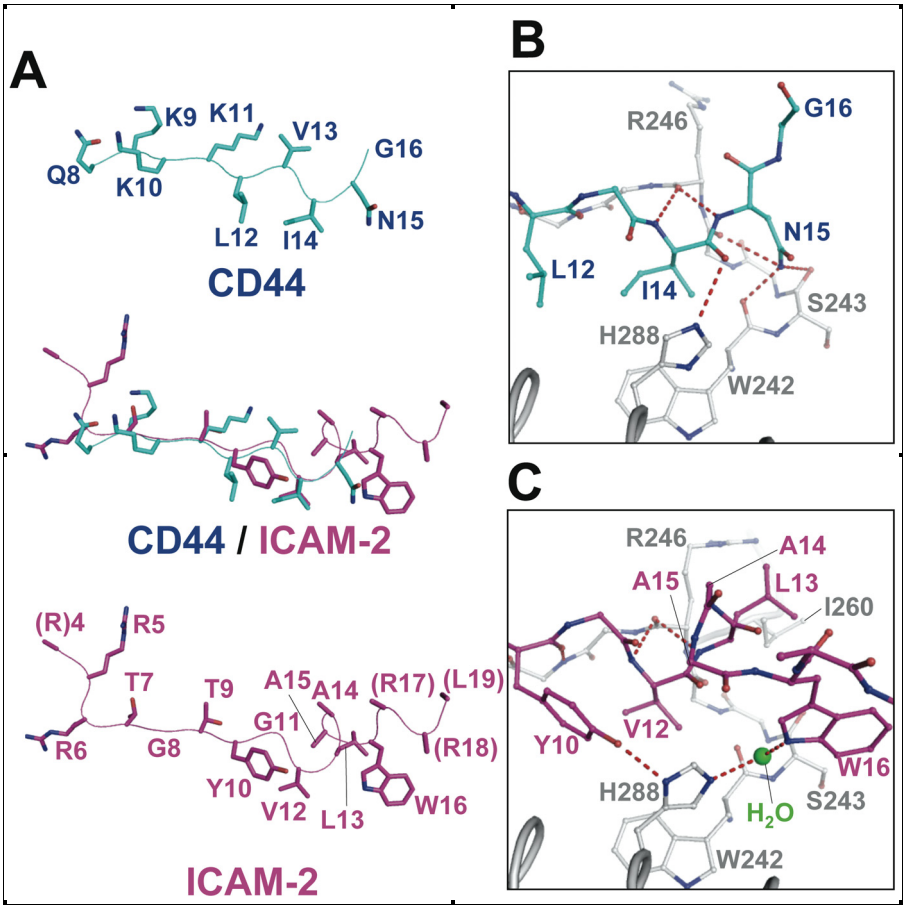

Fig. I-3-10. Comparison of CD44and ICAM-2 peptides bound to the radixin FERM domain.

A, comparison of the FERM-bound peptide conformations of the CD44 (*cyan*) and ICAM-2 (*magenta*) peptides. Two peptide structures are overlaid in the *middle*. The side chains and main chains are shown as *stick and line-tracing models*, respectively.

B, close-up view of the loop region of the CD44 cytoplasmic peptide (*cyan*) bound to the FERM domain (*gray*). The CD44 loop comprising Val13-Ile14-Asn15-Gly16 is docked into pocket *P1* on subdomain C. Hydrogen bonds are shown as *red dashed lines*. The side chain of Val13 is not shown for clarity. CD44 Asn15 forms three hydrogen bonds to the main chain carbonyl groups of Trp242, Ser243, and Ile245 of the FERM domain.

C, close-up view of the 3_{10} helix of the ICAM-2 peptide (*magenta*) bound to the FERM domain (*gray*) in the FERM-ICAM-2 complex (28). The 3_{10} helix comprising Val12-Leu13-Ala14-Ala15 is docked into pocket *P1* on subdomain C. The side chain of Ala15 is not shown for clarity. The water molecule mediating the hydrogen bond between ICAM-2 Trp16 and FERM His288 is shown as a *green sphere*.

I-3-6. Comparison with the FERM-NEP complex

Recently, our group reported on the crystal structures of the radixin FERM domain bound to the cytoplasmic peptide of type II membrane protein NEP (31). Despite the opposite chain polarity of the cytoplasmic region, the NEP peptide binds the groove between helix α1C and strand β5C of subdomain C by forming antiparallel β-β associations with strand β5C that overlaps the observed binding site for the CD44 peptide of the current structure. Notably, structure alignment between the CD44 and NEP peptides reveals a better overlap of the corresponding side chain pairs than structural alignment between CD44 and ICAM-2 (Figs. I-3-11, *A* and *B*). This unexpected close overlap is reflected by the CD44 Leu12 and NEP Thr10 pair and the CD44 Ile14 and NEP Ile12 pair, which bind the *S4* site and *P1* pocket, respectively, and the CD44 Asn15 and NEP Asn13 pair. In the case of NEP, the β strand formed by the MDIT sequence is followed by a hairpin-like structure of the DINA sequence (Fig. I-3-9 *B*). The sharp hairpin structure of NEP slightly shifts the Asn13 side chain from a position occupied by CD44 Asn15 away from the FERM domain (Fig. I-3-11*B*). This shift results in fewer hydrogen bonds being formed between the NEP Asn13 side chain and loop β6C-β7C of the FERM domain (Fig. I-3-11*C*). Instead, the NEP hairpin is stabilized by formation of an additional hydrogen bond between the main chain of NEP Asn13 and the side chain of Arg246 from strand β5C (Fig. I-3-11*C*). Notwithstanding the aforementioned deviations in the intermolecular interactions between the FERM-CD44 and FERM-NEP complexes, the overall binding mode of the CD44 peptide resembles more closely that of the NEP peptide rather than the ICAM-2 peptide. The previous mutation

studies based on the complexed structure identified the NEP signature sequence MXITXIN (Motif-1β), which is distinct from Motif-1 of ICAM-2 (31). The sequence of this motif is less conserved in CD44, whereas the Ile-Asn sequence is conserved in CD44 and plays a role in the binding as mentioned above (Fig. I-3-11*B*).

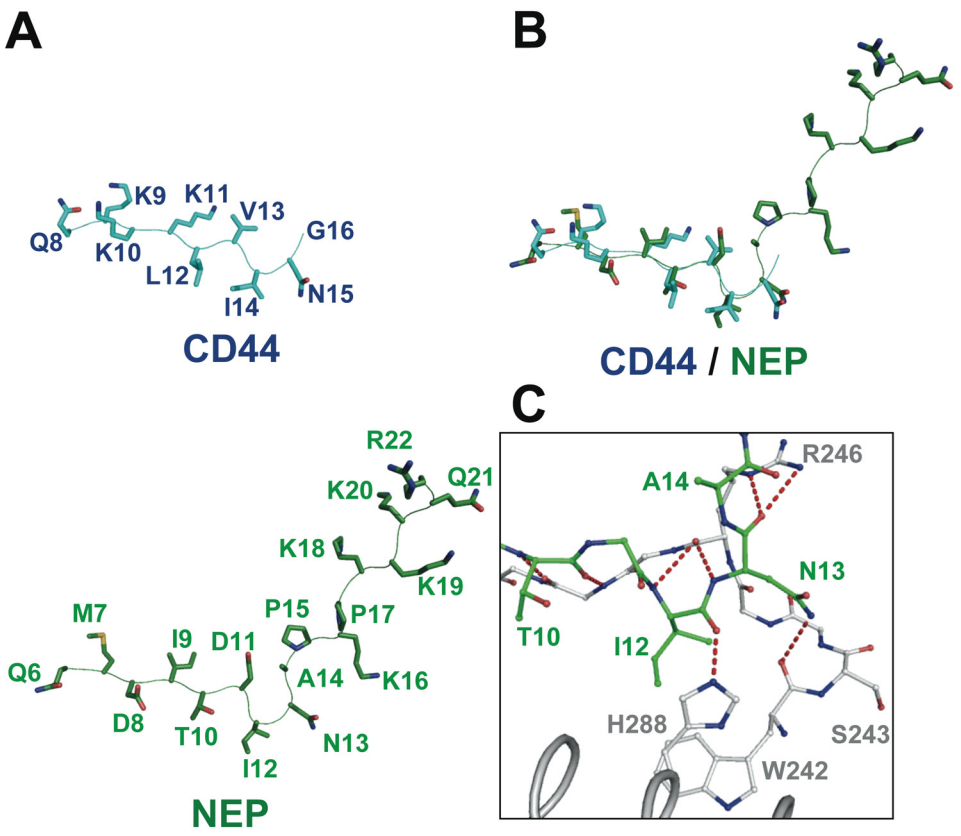

Fig. I-3-11. Comparison of CD44 and NEP peptides bound to the FERM domain.

A, comparison of the FERM-bound peptide conformations of the CD44 (*cyan*) and NEP (*green*) peptides. The side chains and main chains are shown as *stick and line-tracing models*, respectively.

B, two peptide structures are overlaid. *C*, close-up view of the hairpin of the NEP peptide (*green*) bound to the FERM domain (*gray*). The hairpin comprising Asp11-Ile12-Asn13-Ala14 is docked into pocket *P1* on subdomain C. NEP Asn13 forms a hydrogen bond to the main chain carbonyl group of FERM Trp242

I-3-7. Influence of Ser2 phosphorylation on the binding of CD44 peptide to the radixin FERM domain

Previously, Ser291 (Ser2 in the current numbering) of the human CD44 cytoplasmic region was found to be phosphorylated by protein kinase C (44). Interestingly, a point mutation to aspartic acid, which mimics the phosphorylated side chain, was also shown to reduce the interaction with ezrin *in vitro* using cell lysates and *in vivo*, as determined by fluorescence lifetime imaging microscopy. I attempted pull down assays using purified radixin FERM domain and CD44 peptides to test whether phosphorylation of Ser2 interferes with the FERM-CD44 interaction. In the pull-down assay, the binding affinity of the radixin FERM domain to the CD44 peptide having an S2D mutation was reduced by 52%, and that of the radixin FERM domain to the Ser2-phosphorylated CD44 peptide was reduced by 70% in comparison with the affinity to wild-type CD44 peptide (Fig. I-3-12), demonstrating that Ser2 phosphorylation indeed interferes with the interaction between the CD44 peptide and the radixin FERM domain, although Ser2 exhibits no direct interaction with the FERM domain in the structure.

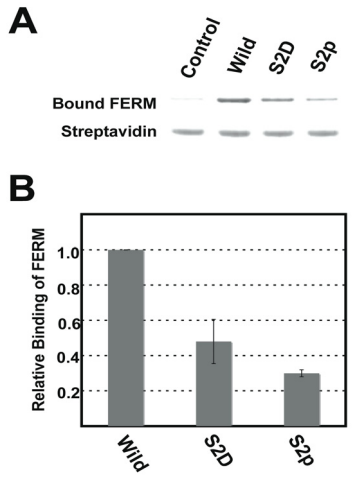

Fig. I-3-12. Pull-down assays of the FERM domain with wild-type and phosphorylated CD44 peptide.
A, eluted samples analyzed by SDS-PAGE. Ser2 is replaced with Asp (*S2D*) and phosphoserine (*S2p*).
B, summary of pull-down assays of wild-type and phosphorylated CD44 to the radixin FERM domain. The *bar graph* documents the relative binding affinity.

I-4. Discussion

The present structural and biophysical characterization of the CD44 cytoplasmic peptide provides several clues concerning the physiological role of the CD44 cytoplasmic peptide and ERM proteins. The hydrodynamic studies clearly show that the full-length CD44 cytoplasmic region is present as an extended monomeric form in solution. Projection of the extended cytoplasmic region from the inner plasma membrane allows for effective binding to multiple proteins containing ERM proteins, ankyrin, and guanine nucleotide exchange factors of the Rho family, such as Tiam1/2 (T-lymphoma invasion and metastasis 1 and 2) (45–47).

I showed that CD44 binds the same binding site on subdomain C of the FERM domain as that of Motif-1, whereas the CD44 sequence of the binding site, KKKLVIN, is distinct from Motif-1. This versatility of peptide recognition by subdomain C is in sharp contrast with that observed for the PTB domains. Most of the PTB domains recognize the NPXY (Y is usually a phosphotyrosine) motif (48, 49), and some recognize the GPY or QVTVS motifs (50, 51), whereas none of the PTB domains recognize both the NPXY and GPY or QVTVS motifs. In some other PTB domains, the peptide wraps around the domain by sitting on the β-sheet comprising β5-β6-β7-β1 strands (32, 51). However, no such interaction has been found to date in the FERM domains of ERM proteins and merlin.

Several factors influence the ability of CD44 to bind hyaluronan of extracellular matrix. These include the expression level of CD44 and posttranslational modifications, such as glycosylation of the extracellular domain. However, a frequently asked question with respect to CD44 activation concerns whether

intracellular events can modulate ligand binding, referred to as “inside-out signaling.” Colocalization of CD44 with activated ERM proteins correlates with hyaluronan binding (24). This binding activity requires the CD44 cytoplasmic region and its ERM-binding site (21, 24, 52). Interestingly, artificial dimerization abolishes this requirement, suggesting that the role of the cytoplasmic region may be to promote CD44 clustering (53). Thus, it has been a fascinating question to consider whether CD44 possesses an intrinsic ability to form dimers and/or oligomers that contribute to localization and clustering, a process believed to have physiological importance in regulating hyaluronan binding avidity (54). However, the hydrodynamic studies are substantial enough for us to speculate that the cytoplasmic region might possess no such ability to initiate dimerization or clustering by self-association. Clustering and oligomerization of CD44 are probably induced by interactions with ERM and other proteins that mediate a mechanical link of the tail to actin cytoskeletons. Notably, the extracellular hyaluronan-binding domain (HABD) of CD44 adopts a monomeric form, which is able to bind hyaluronan (55). I speculate that clustering of CD44 by ERM proteins could accelerate HABD dimerization, which facilitates increased hyaruronan binding. HABD dimerization is also induced by superagonist antibodies whose epitopes were mapped on the HABD surface (56).

As in the case of amyloid β precursor and Notch, it has been shown that CD44 is subject to regulated proteolytic cleavage via a regulated intramembrane proteolysis (RIP) pathway to initiate the CD44-mediated intracellular signaling pathway (57). CD44 cleavage by presenilin-1/γ-secretase can generate the ICD fragment encompassing the whole cytoplasmic region in addition to the secreted extracellular domain fragment (26, 58, 59). Translocation of the ICD fragment into

the nucleus is an essential step for transcriptional activation, which provides a feedback mechanism for regulating CD44 expression (26). Since the CD44 cytoplasmic region is anchored to actin cytoskeletons by binding to ERM proteins, the cleaved cytoplasmic region should be released from ERM proteins prior to nuclear transport, implying that the RIP pathway of CD44 may be coupled with the regulation of ERM proteins. One possible mechanism of release from ERM proteins involves phosphorylation of Ser2 of the CD44 cytoplasmic region by protein kinase C, which reduces CD44 binding to ERM proteins. Protein kinase C is activated by phorbol esters, and, in turn, the transcription of genes controlled by phorbol ester-responsive elements is mediated by the ICD fragment. Thus, positive feedback involving CD44 phosphorylation may regulate CD44 outside-in signaling. In the complex structure, Ser2 is located at the disordered N-terminal 6 residues and is not expected to be in direct contact with the FERM domain (Fig. I-3-6 *C*). However, I point out that Ser2 is located near the two basic clusters RRR and KKK and speculate that the negative charges of phosphorylated Ser2 would strongly interact with the positive charges of the basic residues (Fig. I-3-9 *A*). Since the second basic cluster KKK is part of the FERM-binding site, the postulated electrostatic interactions may destroy the KKK strand structure, thereby resulting in diminished CD44-FERM binding.

Another possible mechanism for ICD fragment release from the ERM protein mediated link to cytoskeletons may involve inactivation of ERM proteins. ERM proteins adopt two states, masked and unmasked, and are inactive as a linker in the masked state (60–62). Unmasking is triggered at the plasma membrane by binding of PIP_2 to the FERM domain (37, 63, 64), which allows for subsequent

phosphorylation at the C-terminal tail domain by Rho kinase (65) or protein kinase C (66). All of these cues relating to the activation of ERM proteins, PIP_2 production induced by Ras, and phosphorylation by Rho-kinase and protein kinase C are in parallel with the stimulation of CD44 cleavage, since the reported experimental data show that CD44 cleavage is induced by the activation of Ras and Rho signaling as well as protein kinase C activation (67, 68). Thus, these signaling pathways would not contribute toward triggering ERM inactivation, and it is unlikely that selective inactivation of ERM proteins occurs during the RIP process.

CD44 is a major component of cartilage and modulates Smad1 activation in chondrocytes in embryonic and adult tissues (69). In this process, a functional link exists between CD44 and the signaling cascade of BMP-7 (bone morphogenetic protein-7), a member of the transforming growth factor-β superfamily (70–73). In the BMP-7 pathway, CD44 recruits Smad1 to transforming growth factor receptor, ALK2, and ActR-II at the plasmamembrane by direct binding. Since the Smad1-binding region is mapped to the C-terminal 54 residues of the CD44 cytoplasmic tail, there is no overlap between the ERM and Smad1 binding sites, suggesting that the CD44 cytoplasmic tail bound to ERM proteins is able to bind Smad1.

Another interesting viewpoint concerns the notion that transforming growth factor-β signaling is somehow functionally coupled with the RIP pathway of CD44, since both the IDC fragment and Smad1 act with p300/CBP to regulate transcriptional activation by bone morphogenetic proteins (26, 74). In this case, Smad1 bound to the CD44ICD fragment may translocate into the nucleus and function as accessory modulators of transcriptional regulation. It has been shown that

phosphorylated Smad1 is released from transforming growth factor receptor and binds Smad4, which then translocates into the nucleus. I speculate that the Smad1-CD44ICD complex might bind Smad4 and cooperatively function as a transcriptional activator. Further investigations including the structural analysis of complexes will be required to address this issue.

In conclusion, I carried out biophysical studies to indicate that the 72-residue cytoplasmic region of CD44 is present as a flexible tail that possesses no intrinsic ability to self-associate to form dimers/oligomers. Crystal structure investigation of the FERM-CD44 complex reveals a distinct peptide binding mode of the radixin FERM domain compared with that of ICAM-2 and other Ig family adhesion molecules. Based on the current structure and reported phosphorylation of the N-terminal Ser of the cytoplasmic region, I suggest a possible mechanism by which CD44 is released from ERM-mediated links to the cytoskeleton for nuclear translocation in the RIP pathway. The identified FERM binding site is located away from the binding region for Smad1, which allows for Smad1 interactions with activated CD44 bound to ERM protein and linked to actin cytoskeletons.

I-5. References

1). Toole, B. P., Wight, T. N., and Tammi, M. I. (2002). Hyaluronan-cell interactions in cancer and vascular disease. *J. Biol. Chem.* 277, 4593–4596

2). Tammi, M. I., Day, A. J., and Turley, E. A. (2002). Hyaluronan and homeostasis: a balancing act. *J. Biol. Chem.* 277, 4581–4584

3). Bajorath, J. (2000). Molecular organization, structural features, and ligand binding characteristics of CD44, a highly variable cell surface glycoprotein with multiple functions. *Proteins* 39, 103–111

4). Lesley, J., Hyman, R., and Kincade, P. W. (1993). CD44 and its interaction with extracellular matrix. *Adv. Immunol.* 54, 271–335

5). Martin, T. A., Harrison, G., Mansel, R. E., and Jiang, W. G. (2003). The role of the CD44/ezrin complex in cancer metastasis. *Crit. Rev. Oncol. Hematol.* 46, 165–186

6). Ponta, H., Sherman, L., and Herrlich, P. A. (2003) CD44: from adhesion molecules to signalling regulators. *Nat. Rev. Mol. Cell. Biol.* 4, 33–45

7). Naor, D., Sionov, R. V., and Ish-Shalom, D. (1997). CD44: structure, function, and association with the malignant process. *Adv. Cancer Res.* 71, 241–319

8). Cichy, J., and Pure, E. (2003) . The liberation of CD44. *J. Cell Biol.* 161, 839–843

9). Thorne, R. F., Legg, J. W., and Isacke, C. M. (2004). The role of the CD44 transmembrane and cytoplasmic domains in co-ordinating adhesive and signalling events. *J. Cell Sci.* 117, 373–380

10). Tsukita, S., Oishi, K., Sato, N., Sagara, J., Kawai, A., and Tsukita, S. (1994). ERM family members as molecular linkers between the cell surface glycoprotein

CD44 and actin-based cytoskeletons. *J. Cell Biol.* 126, 391–401

11). Hirao, M., Sato, N., Kondo, T., Yonemura, S., Monden, M., Sasaki, T., Takai, Y., Tsukita, S., and Tsukita, S. (1996). Regulation mechanism of ERM (ezrin/radixin/ moesin) protein/plasma membrane association: possible involvement of phosphatidylinositol turnover and Rho-dependent signaling pathway. *J. Cell Biol.* 135, 37–51

12). Sainio, M., Zhao, F., Heiska, L., Turunen, O., den Bakker, M., Zwarthoff, E., Lutchman, M., Rouleau, G. A., Jääskeläinen, J., Vaheri, A., and Carpén, O. (1997). Neurofibromatosis 2 tumor suppressor protein colocalizes with ezrin and CD44 and associates with actin-containing cytoskeleton. *J. Cell Sci.* 110, 2249–2260

13). Yonemura, S., Hirao, M., Doi, Y., Takahashi, N., Kondo, T., Tsukita, S., and Tsukita, S. (1998). Ezrin/Radixin/Moesin (ERM) Proteins Bind to a Positively Charged Amino Acid Cluster in the Juxta-Membrane Cytoplasmic Domain of CD44, CD43, and ICAM-2. *J. Cell Biol.* 140, 885–895

14). Tsukita, S., and Yonemura, S. (1999). Cortical Actin Organization: Lessons from ERM (Ezrin/Radixin/Moesin) Proteins. *J. Biol. Chem.* 274, 34507–34510

15). McClatchey, A. I. (2003). Merlin and ERM proteins: unappreciated roles in cancer development? *Nat. Rev. Cancer* 3, 877–883

16). Bonilha, V. L., Finnemann, S. C., and Rodriguez-Boulan, E. (1999). Ezrin Promotes Morphogenesis of Apical Microvilli and Basal Infoldings in Retinal Pigment Epithelium. *J. Cell Biol.* 147, 1533–1548

17). Yonemura, S., Tsukita, S., and Tsukita, S. (1999). Direct Involvement of Ezrin/Radixin/Moesin (ERM)-binding Membrane Proteins in the Organization of Microvilli in Collaboration with Activated ERM Proteins. *J. Cell Biol.*

145,1497–1509

18). Zohar, R., Suzuki, N., Suzuki, K., Arora, P., Glogauer, M., McCulloch,C. A., and Sodek, J. (2000). Intracellular osteopontin is an integral component of the CD44-ERM complex involved in cell migration. *J. Cell. Physiol.* 184, 118–130

19). Lee, J. H., Katakai, T., Hara, T., Gonda, H., Sugai, M., and Shimizu, A. (2004). Roles of p-ERM and Rho–ROCK signaling in lymphocyte polarity and uropod formation. *J. Cell Biol.* 167, 327–337

20). Cywes, C., and Wessels, M. R. (2001). Group A Streptococcus tissue invasion by CD44-mediated cell signalling. *Nature* 414, 648–652

21). Lesley, J., He, Q., Miyake, K., Hamann, A., Hyman, R., and Kincade, P. W. (1992). Requirements for hyaluronic acid binding by CD44: a role for the cytoplasmic domain and activation by antibody. *J. Exp. Med.* 175, 257–266

22). Thomas, L., Byers, H. R., Vink, J., and Stamenkovic, I. (1992). CD44H regulates tumor cell migration on hyaluronate-coated substrate. *J. Cell Biol.* 118, 971–977

23). Mori, H., Tomari, T., Koshikawa, N., Kajita, M., Itoh, Y., Sato, H., Tojo, H., Yana, I., and Seiki, M. (2002). CD44 directs membrane-type 1 matrix metalloproteinase to lamellipodia by associating with its hemopexin-like domain. *EMBO J.* 21, 3949–3959

24). Brown, K. L., Birkenhead, D., Lai, J. C., Li, L., Li, R., and Johnson, P. (2005). Regulation of hyaluronan binding by F-actin and colocalization of CD44 and phosphorylated ezrin/radixin/moesin (ERM) proteins in myeloid cells. *Exp. Cell Res.* 303, 400–414

25). Brown, M. S., Ye, J., Rawson, R. B., and Goldstein, J. L. (2000). Regulated intramembrane proteolysis: a control mechanism conserved from bacteria to humans.

Cell 100, 391–398

26). Okamoto, I., Kawano, Y., Murakami, D., Sasayama, T., Araki, N., Miki, T., Wong, A. J., and Saya, H. (2001). Proteolytic release of CD44 intracellular domain and its role in the CD44 signaling pathway. *J. Cell Biol.* 155, 755–762

27). Bretscher, A., Edwards, K., and Fehon, R. G. (2002). ERM proteins and merlin: integrators at the cell cortex. *Nat. Rev. Mol. Cell. Biol.* 3, 586–599

28). Hamada, K., Shimizu, T., Yonemura, S., Tsukita, S., Tsukita, S., and Hakoshima, T. (2003). Structural basis of adhesion-molecule recognition by ERM proteins revealed by the crystal structure of the radixin-ICAM-2 complex. *EMBO J.* 22, 502–514

29). Takai, Y., Kitano, K., Terawaki, S., Maesaki, R., and Hakoshima, T. (2007). Structural basis of PSGL-1 binding to ERM proteins. *Genes Cells* 12, 1329–1338

30). Terawaki, S., Maesaki, R., and Hakoshima, T. (2006). Structural basis for NHERF recognition by ERM proteins. *Structure* 14, 777–789

31). Terawaki, S., Kitano, K., and Hakoshima, T. (2007). Structural Basis for Type II Membrane Protein Binding by ERM Proteins Revealed by the Radixin-neutral Endopeptidase 24.11 (NEP) Complex. *J. Biol. Chem.* 282, 19854–19861

32). Wegener, K. L., Partridge, A. W., Han, J., Pickford, A. R., Liddington, R. C., Ginsberg, M. H., and Campbell, I. D. (2007). Structural basis of integrin activation by talin. *Cell* 128, 171–182

33). Hamada, K., Matsui, T., Tsukita, S., Tsukita, S., and Hakoshima, T. (2000a). Crystallographic characterization of the membrane-binding domain of radixin. *Acta Crystallogr. Sect. D Biol. Crystallogr.* 56, 922–923

34). Mori, T., Kitano, K., Terawaki, S., Maesaki, R., and Hakoshima, T. (2007).

Crystallographic characterization of the radixin FERM domain bound to the cytoplasmic tail of adhesion molecule CD44. *Acta Crystallogr. F Struct. Biol. Crystalliz. Comm.* 63, 844–847

35). Otwinowski, Z., and Minor, W. (1997). Processing of X-ray diffraction data collected in oscillation mode. *Methods Enzymol.* 276, 307–326

36). McCoy, A. J., Grosse-Kunstleve, R. W., Storoni, L. C., and Read, R. J. (2005). Likelihood-enhanced fast translation functions. *Acta Crystallogr. Sect. D Biol. Crystallogr.* 61, 458–464

37). Hamada, K., Shimizu, T., Matsui, T., Tsukita, S., and Hakoshima, T. (2000). Structural basis of the membrane-targeting and unmasking mechanisms of the radixin FERM domain. *EMBO J.* 19, 4449–4462

38). Jones, T. A., Zou, J. Y., Cowan, S. W., and Kjeldgaard, M. (1991). Improved methods for building protein models in electron density maps and the location of errors in these models. *Acta Crystallogr. Sect. A* 47, 110–119

39). Brünger, A. T., Adams, P. D., Clore, G. M., DeLano, W. L., Gros, P., Grosse-Kunstleve, R. W., Jiang, J. S., Kuszewski, J., Nilges, M., Pannu, N. S., Read, R. J., Rice, L. M., Simonson, T., and Warren, G. L. (1998). Crystallography & NMR system: A new software suite for macromolecular structure determination. *Acta Crystallogr. Sect. D Biol. Crystallogr.* 54, 905–921

40). Pearson, M. A., Reczek, D., Bretscher, A., and Karplus, P. A. (2000). Structure of the ERM protein moesin reveals the FERM domain fold masked by an extended actin binding tail domain. *Cell* 101, 259–270

41). Shimizu, T., Seto, A., Maita, N., Hamada, K., Tsukita, S., Tsukita, S., and Hakoshima, T. (2002). Structural Basis for Neurofibromatosis Type 2. *J. Biol. Chem.*

277, 10332–10336

42). Davis, I. W., Leaver-Fay, A., Chen, V. B., Block, J. N., Kapral, G. J., Wang, X., Murray, L. W., Arendall, W. B., 3rd, Snoeyink, J., Richardson, J. S., and Richardson, D. C. (2007). MolProbity: all-atom contacts and structure validation for proteins and nucleic acids. *Nucleic Acids Res*. 35, W375–W383

43). Collaborative Computational Project, N. (1994). The CCP4 suite: programs for protein crystallography. *Acta Crystallogr. Sect. D Biol. Crystallogr*. 50, 760–763

44). Legg, J. W., Lewis, C. A., Parsons, M., Ng, T., and Isacke, C. M. (2002). A novel PKC-regulated mechanism controls CD44 ezrin association and directional cell motility. *Nat. Cell Biol*. 4, 399–407

45). Lokeshwar, V. B., and Bourguignon, L. Y. (1991). Post-translational protein modification and expression of ankyrin- binding site(s) in GP85 (Pgp-1/CD44) and its biosynthetic precursors during T-lymphoma membrane biosynthesis. *J. Biol. Chem*. 266, 17983–17989

46). Bourguignon, L. Y., Zhu, H., Shao, L., and Chen, Y. W. (2000). CD44 Interaction with Tiam1 Promotes Rac1 Signaling and Hyaluronic Acid-mediated Breast Tumor Cell Migration. *J. Biol. Chem*. 275, 1829–1838

47). Oliferenko, S., Kaverina, I., Small, J. V., and Huber, L. A. (2000). Hyaluronic Acid (HA) Binding to CD44 Activates Rac1 and Induces Lamellipodia Outgrowth. *J. Cell Biol*. 148, 1159–1164

48). Eck, M. J., Dhe-Paganon, S., TruÅNb, T., Nolte, R. T., and Shoelson, S. E. (1996). Structure of the IRS-1 PTB domain bound to the juxtamembrane region of the insulin receptor. *Cell* 85, 695–705

49). Garcia-Alvarez, B., de Pereda, J. M., Calderwood, D. A., Ulmer, T. S., Critchley,

D., Campbell, I. D., Ginsberg, M. H., and Liddington, R. C. (2003). Structural determinants of integrin recognition by talin. *Mol. Cell* 11, 49–58

50). Li, S.-C., Zwahlen, C., Vincent, S. J., McGlade, C. J., Kay, L. E., Pawson, T., and Forman-Kay, J. D. (1998). Structure of a Numb PTB domain-peptide complex suggests a basis for diverse binding specificity. *Nat. Struct. Biol.* 5, 1075–1083

51). Dhalluin, C., Yan, K. S., Plotnikova, O., Lee, K. W., Zeng, L., Kuti, M., Mujtaba, S., Goldfarb, M. P., and Zhou, M. M. (2000). Structural basis of SNT PTB domain interactions with distinct neurotrophic receptors. *Mol. Cell* 6, 921–929

52). Liu, D., Zhang, D., Mori, H., and Sy, M.S. (1996). Binding of CD44 to hyaluronic acid can be induced by multiple signals and requires the CD44 cytoplasmic domain. *Cell. Immunol.* 174, 73–83

53). Perschl, A., Lesley, J., English, N., Trowbridge, I., and Hyman, R. (1995). Role of CD44 cytoplasmic domain in hyaluronan binding. *Eur. J. Immunol.* 25, 495–501

54). Lesley, J., Hascall, V., Tammi, M., and Hyman, R. (2000). Hyaluronan Binding by Cell Surface CD44. *J. Biol. Chem.* 275, 26967–26975

55). Banerji, S., Wright, A. J., Noble, M., Mahoney, D. J., Campbell, I. D., Day,A. J., and Jackson, D. G. (2007). Structures of the Cd44-hyaluronan complex provide insight into a fundamental carbohydrate-protein interaction. *Nat. Struct. Mol. Biol.* 14, 234–239

56). Teriete, P., Banerji, S., Noble, M., Blundell, C. D., Wright, A. J., Pickford, A. R., Lowe, E., Mahoney, D. J., Tammi, M. I., Kahmann, J. D., Campbell, I. D., Day, A. J., and Jackson, D. G. (2004). Structure of the regulatory hyaluronan binding domain in the inflammatory leukocyte homing receptor CD44. *Mol. Cell* 13, 483–496

57). Nagano, O., and Saya, H. (2004). Mechanism and biological significance of

CD44 cleavage. *Cancer Sci*. 95, 930–935

58). Lammich, S., Okochi, M., Takeda, M., Kaether, C., Capell, A., Zimmer, A. K., Edbauer, D., Walter, J., Steiner, H., and Haass, C. (2002). Mechanism and biological significance of CD44 cleavage. *J. Biol. Chem*. 277, 44754–44759

59). Murakami, D., Okamoto, I., Nagano, O., Kawano, Y., Tomita, T., Iwatsubo, T., de Strooper, B., Yumoto, E., and Saya, H. (2003). Presenilin-dependent Intramembrane Proteolysis of CD44 Leads to the Liberation of Its Intracellular Domain and the Secretion of an Abeta -like Peptide. *Oncogene* 22, 1511–1516

60). Gary, R., and Bretscher, A. (1995). Ezrin self-association involves binding of an N-terminal domain to a normally masked C-terminal domain that includes the F-actin binding site. *Mol. Biol. Cell* 6, 1061–1075

61). Ishikawa, H., Tamura, A., Matsui, T., Sasaki, H., Hakoshima, T., Tsukita, S., and Tsukita, S. (2001). Structural conversion between open and closed forms of radixin: low-angle shadowing electron microscopy. *J. Mol. Biol*. 310, 973–978

62). Li, Q., Nance, M. R., Kulikauskas, R., Nyberg, K., Fehon, R., Karplus, P. A., Bretscher, A., and Tesmer, J. J. (2007). Self-masking in an intact ERM-merlin protein: an active role for the central alpha-helical domain. *J. Mol. Biol*. 365, 1446–1459

63). Fievet, B. T., Gautreau, A., Roy, C., Del Maestro, L., Mangeat, P., Louvard, D., and Arpin, M. (2004). Phosphoinositide binding and phosphorylation act sequentially in the activation mechanism of ezrin. *J. Cell Biol*. 164, 653–659

64). Yonemura, S., Matsui, T., Tsukita, S., and Tsukita, S. (2002). Rho-dependent and -independent activation mechanisms of ezrin/radixin/moesin proteins: an essential role for polyphosphoinositides in vivo. *J. Cell Sci*. 115, 2569–2580

65). Matsui, T., Maeda, M., Doi, Y., Yonemura, S., Amano, M., Kaibuchi, K., Tsukita, S., and Tsukita, S. (1998). Rho-Kinase Phosphorylates COOH-terminal Threonines of Ezrin/Radixin/Moesin (ERM) Proteins and Regulates Their Head-to-Tail Association. *J. Cell Biol.* 140, 647–657

66). Pietromonaco, S. F., Simons, P. C., Altman, A., and Elias, L. (1998). Protein Kinase C-θ Phosphorylation of Moesin in the Actin-binding Sequence. *J. Biol. Chem.* 273, 7594–7603

67). Okamoto, I., Kawano, Y., Tsuiki, H., Sasaki, J., Nakao, M., Matsumoto, M., Suga, M., Ando, M., Nakajima, M., and Saya, H. (1999). CD44 cleavage induced by a membrane-associated metalloprotease plays a critical role in tumor cell migration. *Oncogene* 18,1435–1446

68). Kawano, Y., Okamoto, I., Murakami, D., Itoh, H., Yoshida, M., Ueda, S., and Saya, H. (2000). Ras Oncoprotein Induces CD44 Cleavage through Phosphoinositide 3-OH Kinase and the Rho Family of Small G Proteins. *J. Biol. Chem.* 275, 29628–29635

69). Peterson, R. S., Andhare, R. A., Rousche, K. T., Knudson, W., Wang, W., Grossfield, J. B., Thomas, R. O., Hollingsworth, R. E., and Knudson, C. B. (2004). CD44 modulates Smad1 activation in the BMP-7 signaling pathway. *J. Cell Biol.* 166, 1081–1091

70). Moustakas, A., Souchelnytskyi, S., and Heldin, C.H. (2001). Smad regulation in TGF-beta signal transduction. *J. Cell Sci.* 114, 4359–4369

71). Tsukazaki, T., Chiang, T. A., Davison, A. F., Attisano, L., and Wrana, J. L. (1998). SARA, a FYVE domain protein that recruits Smad2 to the TGFbeta receptor. *Cell* 95, 779–791

72). Wu, G., Chen, Y. G., Ozdamar, B., Gyuricza, C. A., Chong, P. A., Wrana, J. L., Massagué, J, J., and Shi, Y. (2000). Structural Basis of Smad2 Recognition by the Smad Anchor for Receptor Activation. *Science* 287, 92–97

73). Sasaki, A., Masuda, Y., Ohta, Y., Ikeda, K., and Watanabe, K. (2001). Filamin Associates with Smads and Regulates Transforming Growth Factor-β Signaling. *J. Biol. Chem.* 276, 17871–17877

74). Pouponnot, C., Jayaraman, L., and Massagué, J. (1998). Physical and Functional Interaction of SMADs and p300/CBP. *J. Biol. Chem.* 273, 22865–22868

II. EB1-CLASP complex

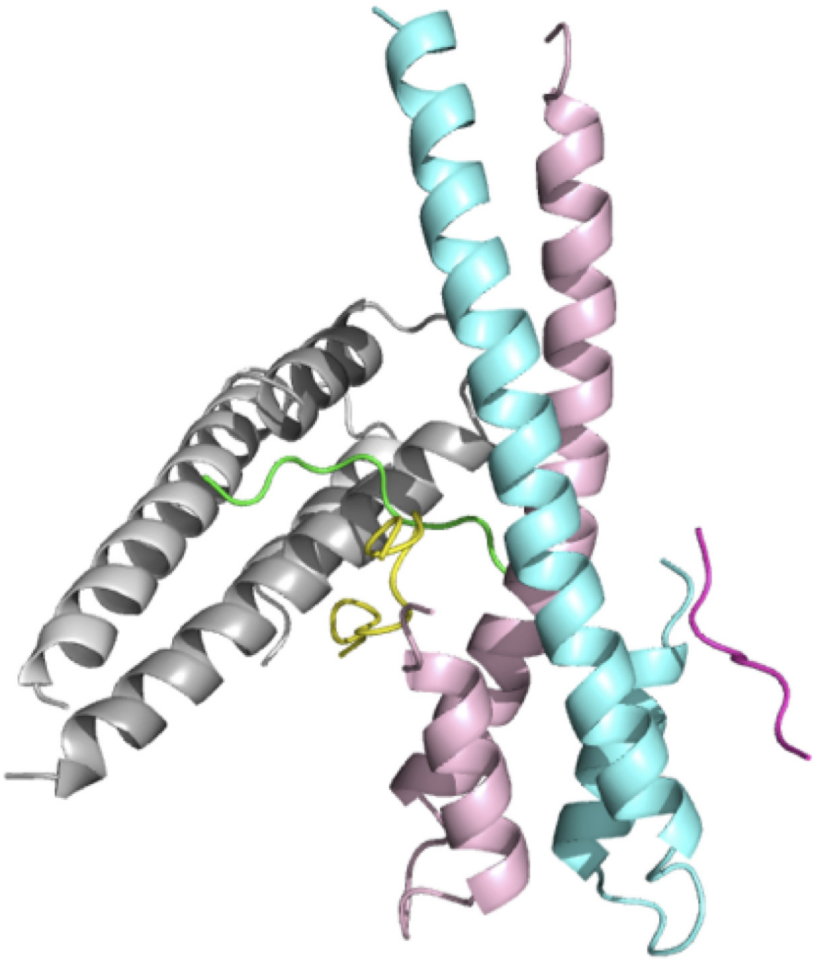

II-1. Introduction

II-1-1. Microtubule plus end tracking proteins (+TIPs)

The microtubule (MT) is one of the major cytoskeleton in all eukaryotic cells. MT is composed of α/β-tubulin heterodimers. α/β-tubulins are polymerized for binding head to tail to form a MT-protofilament, and ~13 MT-protofilaments aligned in parallel produce a cylindrically hollow tube. *In vivo* and *in vitro*, MTs can switch stochastically between growing and shrinking phases, which are produced by the α/β-tubulin polymerization or depolymerization at MT ends, and this phenomenon is known as MT dynamic instability. MT possesses two ends, the slow-growing (minus) and the fast growing (plus) ends. In living cells, MT minus ends are often stabilized and connected with the microtubule organization center (MTOC) such as the centrosome, while MT plus ends extend from MTOC toward the cellular space and cell cortex with behaving dynamic instability (1,2). Therefore, it is important for the orientation of MTs and the establishment of the cell polarity to regulate the dynamics of MT plus ends and their interactions with other cellular components. A great number of MT associating protein (MAP) regulate MT dynamic instability and consequently determine the shape of MT network in the cells.

Recently, some MAPs that specifically accumulate to the growing MT plus ends and regulate MT plus end dynamics have been identified. These MAPs are named microtubule plus end tracking proteins (+TIPs), including members of structurally unrelated protein families, such as the cytoplasmic linker protein 170 kDa (CLIP-170), CLIP-115, ademonatous polyposis coli (APC), end binding protein 1,2,3

(EB1,2,3), $p150^{Glued}$, cytoplasmic linker associated proteins (CLASPs) and microtubule actin crosslinking factor (MACF). +TIPs contain in the MT binding domain in their molecules such as cytoskeleton associated protein Gly rich (CAP-Gly) domain in CLIP-170/115 and $p150^{Glued}$, calponin homology (CH) domain in EB1,2,3 and Ser/Arg/Lys rich region of APC, MACF and CLASPs (3-6). These proteins specifically bind MT plus ends and form a protein-protein interaction network. Thus, +TIPs involved in regulation of MT plus end dynamics and in interactions between MT plus ends and cellular components such as the cell cortex and chromosomes in the cells.

II-1-2. +TIPs, EB1 and CLASP

EB1, initially identified as a binding partner of the tumour suppressor gene product APC (7,8), is a highly conserved member of +TIPs in eukaryotic cells. EB1, Mal3 (EB1 homologue; *Schizosaccharomyces pombe*) and Bim1 (*Saccaromyces cerevisiae*) are localized on MT growing ends both i*n vivo* and *in vitro* and involved in MT dynamics at MT ends (9-13). EB1 is thought to be the master element of +TIPs since EB1 and Mal3 play a role in scaffolding to recruit other +TIPs to growing MT plus ends (9,14-21). The EB1 molecule encompasses four regions; an N-terminal domain, a less conserved linker region, a C-terminal domain and an acidic tail region. The N-terminal domain, which contains calponin homology (CH) domain (22), is the MT binding domain. CH domains are typically found in actin binding proteins (23,24) and also exist in MACF (25,26). The C-terminal domain of EB1 and the acidic tail mainly act as the ‘cargo binding domain’ by associating with other

+TIPs such as CLIP-170/115, p150^{Glued}, APC, MACF and CLASP. The C-terminal domain of EB1 is highly conserved among EB1 protein families and referred to as EB1 domain or EB1 homology domain (EB1-HD) (15). This EB1-HD forms four α-helix bundle structures by parallel dimerization of two EB1 protein monomers (Fig.II-3-2 A) (27,28). The highly conserved hydrophobic residues of the four α-helix bundle structure in EB1-HD dimmer forms two deep hydrophobic pockets. The mutagenesis and binding experiments have indicated that the highly conserved residues forming the hydrophobic pocket are important for binding to APC and MACF, which possess Ile-Pro motif in their molecules. The mutagenesis analysis of APC indicates that the Ile-Pro motif is the essential motif for association between APC and EB1-HD (27-29). The C-terminal acidic tails of EB proteins are flexible and conserved the EEY/F motif of its tail end. This EEY/F motif is recognized by CAP-Gly domain of other +TIPs such as CLIP-170/115 and p150^{Glued} (30,31).

CLASP was originally identified as binding partners of CLIP using yeast two-hybrid analysis, which showed that the CLASP C-terminal domain can bind the CLIP coiled coil domain (32). CLASP has isoforms and CLASP1 is ubiquitously expressed, whereas CLASP2 is expressed in the brain. Both of CLASPs exist as several isoforms, which differ at their N termini. One isoform of CLASP2 has a small N-terminal palmitoylation motif, which is responsible for anchoring the protein to membranes (32). CLASP is homologous to the *D. melanogaster* Orbit/MAST protein. Orbit/MAST was independently identified earlier than CLASP and has been shown to be essential for mitosis in *Drosophila melanogaster* (33,34). The over expression and RNAi knockdown studies show that CLASP is localized at MT plus ends, leading-edge and Golgi apparatus in the cell and involved in stabilizing MT plus end

and capturing MT plus ends to cell cortex, being depended on GSK3β and phosphatidylinositol 3 kinase signaling pathway (32,35,36). Thus, the MT plus ends accumulation of CLASP is the important function for regulating the MT plus end dynamics and forming the MT orientations in the cells. The recent study has shown that CLASP can directly interact with EB1 through the Ser/Arg/Lys rich region and to accumulate to MT plus end and promotes MT plus ends stabilization with colocalized EB1 (35).

II-1-3. Aim of this study

Most +TIPs contain the MT and EB1 binding domains, which are important in accumulation and stabilization of the MT plus end. Increasing evidence indicates that EB1 is involved in CLIP-170 and APC accumulation to MT plus ends (16,29,35). EB1 acts as a scaffold protein to recruit other +TIPs to growing MT plus ends. The EB1 CH domain, which specifically recognizes the sheet and the seam structures of MT (37,38), binds the MT plus end that probably forms the sheet structure of MT (18). Concurrently, the EB1 C-terminal region including the acidic tail is associated with other +TIPs. Thus, the EB1 C-terminal region plays an important role in cargo binding. The biophysical and structural studies shows that the EEY motif localized at the acidic tail end of EB1 is recognized by CAP-Gly domain of CLIP-170 or $p150^{Glued}$, while EB1-HD bind to APC and MACF that contain Ile-Pro motif in their molecules. However, the precise binding mode of CLASP and EB1 is still unclear.

Here, I performed an analysis of EB1-CLASP2γ interaction using pull down

assay. This interaction analysis has showed that CLASP could bind EB1-HD with two CLASP peptide regions in the Ser/Arg/Lys rich region containing the Ser-Lys/Arg-Ile-Pro motif. I also performed tubulin-CLASP2γ interaction analysis using pull down assay and showed that EB1-HB binding peptide regions are overlapped with the tubulin binding region of the Ser/Arg/Lys rich region in CLASP2γ. In addition, I determined the crystal structure of EB1-HD complexed with a CLASP2γ peptide. The EB1-CLASP complex structure illustrates that the Ile-Pro motif in the CLASP peptide is docked into the hydrophobic pocket formed by EB1-HD dimmer and Ser-Lys residues before Ile-Pro motif formed two hydrogen bonds to the side chain of Glu225 from EB1-HD to stabilize the EB1-CLASP interaction. The sequence alignment of other +TIPs comprising Ile-Pro motif in the Ser/Arg/Lys rich region such as APC and MACF implies that the Ser-X-Ile-Pro (where X represents any amino acid) sequence is essential for binding EB1-HD.

II-2. Materials and Methods

II-2-1. Expression and purification of EB1 and CLASP2γ constructs

Human CLASP2γ constructs, residues 340-640 (CLASP-ML), 457-549 (CLASP-MS1), 457-491 (CLASP-MS2), 492-549 (CLASP-MS3), 492-505 (CLASP-rep1), and 515-533 (CLASP-rep2), and mouse EB1 constructs, residues 1-268 (EB1-Full), 1-130 (EB1-CH), 131-190 (EB1-LN), 191-268 (EB1-C), and 191-250 (EB1-HD), were subcloned into pET49b (+) plasmid (Novagen) using the *Sma* I and *EcoR* I restriction enzyme sites. These construct regions are illustrated in Fig. II-3-1. Proteins were expressed in *Rosetta2(DE3)* cells (Novagen) as fusion proteins with glutathione-S-transferase (GST). For multi-wavelength anomalous dispersion (MAD) experiments, EB1Se, which is mutated from Val243 of EB1-HD to Met (28), was constructed using QuickChange (Stratagene). Cells were grown at 37 °C in LB medium containing 50 mg ml^{-1} kanamycin and 50 mg ml^{-1} chloramphenicol, while EB1Se was expressed in *B834(DE3)* cells transformed pRARE2 (Novagen) and cultivated at 37°C in Le Master medium containing 50 mg ml^{-1} kanamycin and 50 mg ml^{-1} chloramphenicol and 50 mg ml^{-1} DL-selenomethionine (SeMet). When OD_{660} of the cell culture reached 0.6, isopropyl β-D-thiogalactopyranoside (IPTG) was added to a concentration of 0.1 m*M* to induce expression of the GST-fused proteins. Cells were grown for an additional 2 hours following IPTG induction and were then collected by centrifugation at 4000 rev min^{-1} (Beckman J2-M1 JA10 rotor) for 15 min at 4°C.

Wet cells expressing GST-fused proteins were suspended in 50 mM Tris

buffer (pH 8.0) containing 500 mM NaCl, 1 m*M* dithiothreitol (DTT) and 1 mM ethylenediamine tetraacetic acid (EDTA) and then disrupted by sonication at 4°C. The soluble fractions of the cell extract were then loaded onto a GSH affinity column of glutathione-Sepharose 4B (GSH) resin (GE Healthcare) and then washed copiously with 5 mM Tris buffer (pH 8.0) containing, 1m*M* DTT, and 1m*M* EDTA. Bound GST fused proteins were cleaved from the GSH resin using 2 units ml^{-1} HRV3C protease (Novagen) for 16h at 4 °C. In the case of GST fused proteins, proteins bound GSH resin were eluted with 5 m*M* Tris buffer (pH 8.0) containing, 1m*M* DTT, 1m*M* EDTA and 20m*M* glutathione reduced form. All GST removed proteins remain GP residues that are part of HEV3C protease recognition site. GST-fused and GST-removed proteins were purified by using a HiTrap SP or HiTrap Q ion-exchange column (GE Healthcare) and a Superdex 200 or 75 gel-filtration column (GE Healthcare) with 10 m*M* HEPES buffer (pH 7.4) containing 150 m*M* NaCl and 1 m*M* DTT. Eluted proteins were concentrated by using Amicno Ultra 3000 MWCO (Millipore). GST-removed CLASP-rep1 peptide was further purified by using a RPC resource column (GE Healthcare), equilibrated with water. The CLASP-rep1 peptide bound to the RPC resource column was eluted with a linier gradient of acetonitrile. The eluted CLASP-rep1 peptide was lyophilized and then dissolved in 10 m*M* HEPES buffer (pH 7.4) containing 1 m*M* DTT. Purified samples were divided into 5-10 μl aliquots in 0.5 ml tubes (Eppendorf) and immediately frozen in liquid nitrogen. Frozen samples were stored at -80 °C until use. The identity of the purified protein was confirmed using MALDI TOF MS (PerSeptive Inc.) and N-terminal sequence analysis (M492; Applied Biosystems).

II-2-2. Interaction analysis using pull down assay

Pull-down assays were performed using GSH resin (GE Healthcare). Bovine α/β-tubulin (tubulin) was purchased from Cytoskeleton, inc (USA). For each reaction, 25 μl of the GSH resin was mixed with 40-100 μg of each GST-fused EB1 or CLASP sample and suspended in 1 ml of 10 m*M* HEPES buffer (pH 7.4) containing 150 m*M* NaCl and 1 m*M* DTT (pull-down buffer) in a 1.5-ml tube (Eppendorf). Resin bound to GST was used as the control. Resin was harvested as a pellet by centrifugation (2000 *g* for 1 min). After removing the supernatant, the resin was suspended in 1 ml of pull-down buffer again, and this wash was repeated two times. 170 μg of CLASP-ML, 150 μg of EB1-HD or 150 μg of tubulin dissolved in the pull-down buffer was added to the resin bound to GST-fused EB1 or GST-fused CLASP2γ, respectively. In the pull-down assay of EB1 and CLASP, each resin was incubated for 1 hour at room temperature with occasional mixing. While in the CLASP-tubulin interaction assay, each resin bound to GST-fused CLASP was incubated for 1 hour at 4 °C. And then, each resin was washed five times with the pull-down buffer by centrifugation. To elute the GST-fused proteins and their associated CLASP-ML, EB1-HD or tubulin, 25 μl of the SDS-sample buffer was added to recovered resin, and then each sample was incubated for 5 min at 96 °C. Eluted proteins were analyzed by SDS-PAGE and visualized using SimplyBlueTM SafeStain (Invitrogen).

II-2-3. Crystallization of the EB1-CLASP complex

The purified EB1-HD and the purified CLASP-rep1 peptide (sequence; GP ^{492}KRSKIPRSQGCSRE^{505}) were mixed in a 1:10 molar ratio [2.5 m*M* EB1-HD and 25 m*M* CLASP-rep1 peptide] with 10 m*M* HEPES buffer (pH 7.4) containing 1 m*M* DTT (EB1-CLASP solution). N-terminal GP residues in CLASP-rep1 is the linker region of HRV3C recognition site for removing GST tag. The initial screening of crystallization conditions was carried out with the sitting-drop vapor-diffusion method at 20 °C using a HYDRA II Plus One crystallization robot (Matrix Technology) and commercial crystallization screening kits (HAMPTON; Crystal screen HT and Index, Qiagen; PEGs I, PEGs II, Anion, Cation, $AmSO_4$, and PACT suite). The EB1-HD complexed with the CLASP-rep1 peptide crystals (EB1-CLASP complex crystals) were obtained within 10 days by mixing 0.2 μl of protein solution 1 with 0.2 μl of the Index suite reservoir solution No. E6 [0.1 *M* bis-Tris buffer pH 6.5 containing 30% polyethylene glycol 550 MME (PEG550MME) and 0.2 *M* calcium chloride]. Crystallization conditions were then refined by changing pH (between 6.0 and 7.5 in increments of 0.1) and the concentration of PEG550MME (40-35 % in 1% increments) using the hanging-drop vapor-diffusion method at 20 °C. The solutions used for the optimized crystallization conditions were prepared by mixing 2.5 μl of the EB1-CLASP solution with 2.5 μl of each reservoir solution. EB1-CLASP crystals were obtained within 10 days (Fig. II-2-1). For the MAD method, EB1Se complexed with CLASP-rep1 crystals (EB1Se-CLASP complex crystals) were obtained by using essentially the same method for the EB1-CLASP complex crystals.

II-2.4. X-ray diffraction data collection of the crystals

Crystals for diffraction studies were transferred stepwise into a cryoprotective solution consisting of 0.05 *M* HEPES buffer pH 7.4 containing 0.1 *M* $CaCl_2$, 40% PEG550MME for flash-cooling. Diffraction tests were performed using an in-home X-ray generator (Rigaku FR-E) equipped with a Rigaku R-AXIS VII detector at -170 °C. X-ray diffraction data for structure determination were collected from the EB1-CLASP complex crystals by using a Rigaku ADSC Quantum 315 detector installed on beamline BL41XU at SPring-8, (Harima, Japan). Crystal data of the EB1-CLASP complex and the intensity data statistics are summarized in Table II-2-2. Diffracted x-ray intensities were processed using the HKL-2000 program suite (39). The MAD data collection of the EB1Se-CLASP complex crystals was performed using a Rayonix MX225 detector installed on beamline BL41XU at SPring-8. Statistics of the MAD data set of the EB1Se-CLASP crystals and the intensity data statistics are summarized in Table II-2-1.

II-2.5. Structural determination and refinement of the EB1-CLASP complex

Phases of the EB1Se-CLASP complex were determined by MAD method. X-ray fluorescence was used to detect and confirm the presence of selen (Se) atoms in the crystals in addition to determining the peak, inflection points of the Se *K* edge and the remote for MAD data collection. Automated phasing of the MAD X-ray data using the autoSHARP program (40) allowed the identification of three Se atoms in the asymmetric unit. These Se atom positions were used for obtaining initial phases

with a figure of merit of 0.332/0.339 (acentric/centric) at 3.1 Å resolution. The initial electron density maps confirmed the presence of three EB1 molecules in the asymmetric unit. The initial model of EB1 molecules was built by using the graphic program COOT (41) and used as the initial model for structural refinement and map calculation at 2.6 Å resolution. The calculated maps showed definite residual electron densities for the CLASP-rep1 peptides both on $|2Fo - Fc|$ and $|Fo - Fc|$ maps. Three CLASP-rep1 peptides bound to EB1-HD were built manually by using the COOT. The EB1-CLASP complex structure was refined manually by using the COOT, the restraint least-squares refinement using the program REFMAC5 (42), rigid-body, simulated annealing, and restrained individual B-factor refinement performed using the program CNS (43). The refinement statistics are summarized in Table II-2-2. The stereo chemical quality of the model was assessed using the program MolProbity (44,45). In the Ramachandran plot, 96.7 and 3.3% of residues were located within the most favored and additional allowed regions, respectively. No residue was found in a disallowed region as defined by the aforementioned program. Molecular illustrations were prepared using the program PyMOL (DeLano Scientific), while molecular surface representations were drawn using the program APBS (46,47).

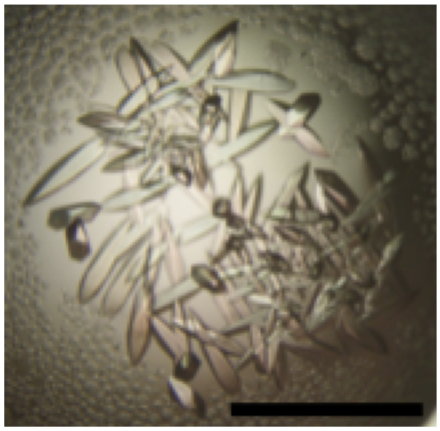

Fig. II-2-1. Crystals of EB1-HD complexed with CLASP-rep1. The scale bar indicates 0.5 mm.

Table II-2-1. MAD data collections of the EB1Se-CLASP complex crystal

Beamline (SPing-8)	BL41XU		
Detector	MX225HE		
Camera distance(mm)	300mm		
Temperature (K)	100		
Oscillation range (°)	180 ° (1° × 180 images)		
Exposure time (s)	0.5 (Al attenuator 400 μm)		
Space group	$P3_221$		
Wavelength (Å)	0.979057 (peak)	0.979364(edge)	0.995084(remote)
Unit-cell *a,b,c* (Å)	60.748, 60.748, 120.694	61.222, 61.222, 121.351	60.813, 60.813, 120.963
Resolution (Å)†	20-3.1 (3.21-3.10)	20-3.1 (3.21-3.10)	20-3.1 (3.21-3.10)
Reflections			
total / unique	48,247 / 4,990	47,178/ 4,963	45,693/ 4,836
Completeness (%)	97.7 (79.1)	96.7 (73.1)	95.8 (69.0)
Mosaicity	0.6 –1.2	0.6 –1.2	0.8-1.3
$< I/ \sigma_I >$	13.0(5.0)	12.5(3.9)	12.6(3.8)
R_{merge} (%)‡	9.0 (31.6)	8.3(35.3)	8.1(38.2)

† Statistics for the outer resolution shell are given in parentheses.
‡ $R_{merge} = \Sigma \mid I_i - < I_i > \mid / \Sigma < I_i >$, where I_i is the observed intensity and $< I_i >$ is the average intensity over symmetry equivalent measurements.

Table II-2-2. Crystallographic and refinement statistics of EB1-CLASP complex crystal

Parameter	Value
X-ray data	
Beamline (SPing-8)	BL41XU
Detector	ADSC Quantum 315
Wavelength (Å)	1.00
Temperature (K)	100
Oscillation range (°)	180° (2° × 90 images)
Exposure time (s)	2
Space group	$P3_221$
Unit-cell parameters *a,b,c* (Å)	60.207 , 60.207, 120.599
Resolution (Å)[a]	20-2.6 (2.59-2.6)
Reflections, total / unique	41,742 / 8,184
Completeness (%)	99.4 (99.9)
Mosaicity	0.52 –0.60
$< I/s_I >$	14.1 (2.5)
R_{merge} (%)[b]	4.1 (54.2)
Refinement	
No. of residues included	
EB1	164 (3 molecules)
CLASP	32 (3 molecules)
Water	54
No. of atoms	1665
R_{work}/R_{free}(%)[c]	25.6 / 28.4
Average B-factor (Å^2)	
EB1	88.6 (3 molecules)
CLASP	87.6 (3 molecules)
Water	74.6
Root mean square	
bond length (Å), angles (degrees)	0.007, 1.2

[a] Statistics for the outer resolution shell are given in parentheses.
[b] $R_{merge} = \Sigma \mid I_i - < I_i > \mid / \Sigma < I_i >$, where I_i is the observed intensity and $< I_i >$ is the average intensity over symmetry equivalent measurements.
[c] $R_{work} = \Sigma \mid \mid F_{obs} \mid - \mid F_{calc} \mid \mid / \Sigma \mid F_{obs} \mid$. R_{free} is the same as R_{work} except for a 5% subset of all reflections that were never used in the crystallographic refinement.

II-3. Results

II-3-1. Pull down assay with CLASP-EB1 and CLASP-tubulin

Recently, the interaction analysis between human EB1 and CLASP2γ has been reported. This report shows that EB1 binds the MT binding domain of CLASP2γ , which is CLASP-M (residues 444-580) region containing the Ser/Arg/Lys residues and is a highly basic region (35). However, the precise mechanism between CLASP and EB1 or CLASP and MT are still unclear. In an effort to address the question of the precise EB1 and MT binding modes of CLASP, I performed the binding assays between CLASP and tubulin or CLASP and EB1 using pull down assay. The peptide regions of CLASP and EB1 using the pull down assay are summarized in Fig. II-3-1 C and D. Pull down assay between GST-fused CLASP and tubulin showed that all CLASP peptides containing 14 residues of CLASP-rep1 bind tubulin. The binding affinity between the GST-fused CLASP peptides and tubulin tended to be weak by shortening the length of CLASP peptides (Fig. II-3-1 F). The observed binding of CLASP to tubulin may be due to electrostatic interactions between the positively charges of the CLASP peptides and the acidic residues on the surface of tubulin molecules. However, the pull down assay between GST-fused CLASP and tubulin showed that EB1-HD specifically binds at the two tandem repeat regions of CLASP2γ, residues 492-505 or 515-533 (Fig. II-3-1 E and F). These repeated sequences of CLASP2γ and the sequence alignment are shown in Fig. II-3-5. This result suggests that CLAPS2γ encompasses two EB1-HD binding regions, CLASP-rep1 and CLASP-rep2, in CLASP-M.

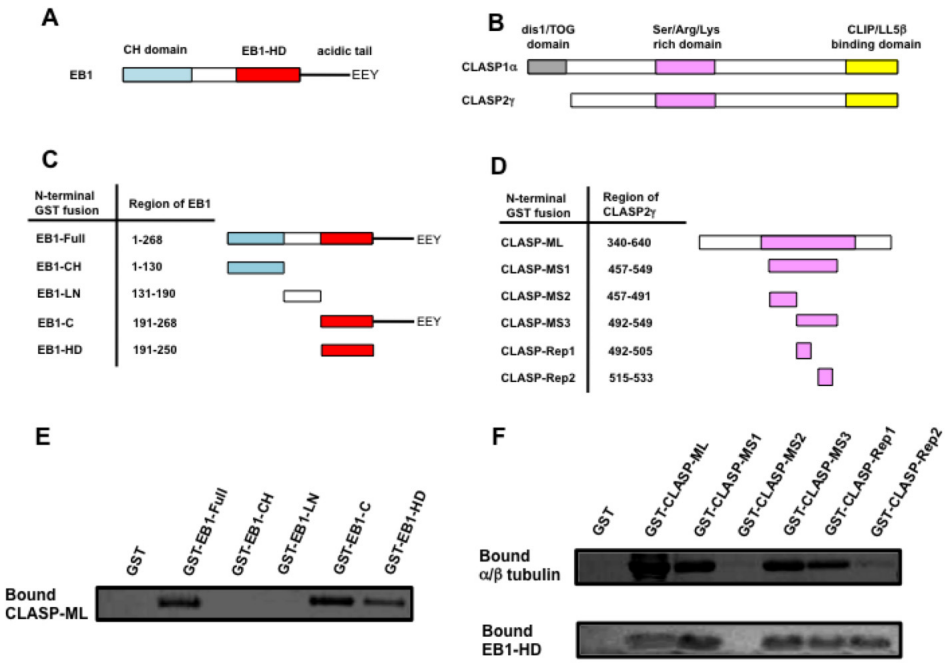

Fig. II-3-1. Interaction analysis of between EB1 and CLASP or CLASP and EB1 using pull down assay

A. Domain organization of mouse EB1. The calponin homology (CH) domain and EB1 homology domain (EB1-HD) are shown by blue and red, respectively. CH domain directory bind MT. EB1-HD formed a coiled coil dimmer and the motif EEY at the end of acidic tail act as 'cargo binding domain' for associating with other +TIPs such as CLIP-170/115, p150Glued, APC and MACF (27,28,30,31,62).

B. Domain organization of human CLASP1α and CLASP2γ. N-terminal dis1/TOG domain, middle Ser/Arg rich domain (CLASP-M) and C-terminal CLIP/LL5β binding domain are shown by gray, pink and yellow, respectively. CLASP-M of the EB1/MT binding region have been reported (35).

C. Schematic representation of mouse EB1 constructs used in this study.

D. Schematic representation of human CLASP2γ constructs used in this study.

E. Pull-down assays of GST-fused EB1 constructs with non-tagged CLASP-ML. Eluted samples were analyzed by SDS-PAGE.

F. Pull-down assays of GST-fused CLASP2γ constructs with non-tagged EB1-HD or tubulin. Eluted samples were analyzed by SDS-PAGE. *Upper panel* is shown the pull down assay result between GST fused CLASP constructs and tubulin. *Under panel* is shown the pull down assay result between GST fused CLASP constructs and EB1-HD.

II-3-2. Crystallization and structure determination of the EB1-CLASP complex

CLASP-rep1 (sequence; GP ^{492}KRSKIPRSQGCSRE^{505}) and EB1-HD was used in the crystallization screening experiment since the interaction analysis using the pull down assay indicated that CLASP-rep1 is the most minimum region for binding EB1-HD among CLASP peptides used pull down assay (Fig. II-3-1 F) and purification of CLASP-rep1 was successful. Contrary, CLASP-rep2 purification for obtaining the EB1-HD-CLASP-rep2 complex crystals was unsuccessful because of rapid degradation during purification. The structure of the EB1-CLASP complex was determined by MAD and molecular replacement methods and subsequently refined to 2.6 Å resolution with an *R*-value of 25.6% (and a free *R*-value of 28.4%). The crystal structure in the asymmetric unit is illustrated in Fig.II-3-2 A. The EB1-CLASP complex contained three EB1-HD (Chain-A, B and C) and three CLASP-rep1 peptides (CLASP-rep1 A, B, and C) in the asymmetric unit. Two EB1-HD molecules (EB1-Chain A and B) form a dimmer and one EB1-HD molecule (EB1-Chain C) lie on the crystallographic two-fold axis to form a dimmer with its crystallographically symmetric EB1-HD molecule. Basically, each CLASP-rep1 peptide binds to each EB1-HD domain in a 1:1 molar ratio, whereas one EB1-HD dimmer interacts with two CLASP-rep1 peptides. On the current electron density map, the N-terminal G residue and the C-terminal SQGCSRE residues of CLASP-rep1 A, the C-terminal RE residues of CLASP-rep1 B, and the C-terminal SQGCSRE residues of CLASP-rep1 C were not observed in the electron density map. Furthermore, the N-terminal GPDE of EB1-Chain A, the N-terminal GP of EB1-Chain B and the N-terminal 14 residues of EB1-Chain C on the crystallographic two-fold axis were not observed in the

electron density map.

II-3-3. CLASP recognition by EB1

The structural characteristics of the EB1-HD dimmer have been reported previously with the crystal structures of human EB1-HD (27,28). The sequence identity between human EB1-HD and mouse EB1-HD is 99%. The EB1-HD peptide chains, which comprise two α-helices α1, α2 in one molecule, form a coiled-coil dimmer that contained a four--helix-bundle structure at the C-terminal region (Fig.II-3-2 A). Three CLASP-rep1 peptides associated with the four-helix-bundle region in the EB1-HD dimmer (Fig.II-3-2 A). Among three CLASP-rep1 peptides in the asymmetric unit, the longest CLASP-rep1 peptide model was obtained for CLASP-rep1 B, which encompasses residues 492-503 (Fig.II-3-2 B).

The EB1-CLASP interaction mode is summarized in Fig. II-3-3 C. The side chains of the Ile496-Pro497 motif in the CLASP-rep1 peptide are docked into the deep and wide hydrophobic pocket formed by the hydrophobic residues at the α-helix bundle of the EB1-HD dimmer (Fig.II-3-3 A, B). Around the hydrophobic pocket of EB1-HD, which is docked to CLASP-rep1 Ile496-Pro497 residues, two interaction sites (S1 and S2) are created. The Ser494 side chain of the CLASP-rep1 peptide forms a hydrogen bond with the Glu225 side chain of EB1-HD at the S1 site. The Glu225 side chain of EB1-HD additionally forms a hydrogen bond with the main chain of Lys495 from the CLASP-rep1 peptide. The long side chain of Lys495 from the CLASP-rep1 peptide sticks to the Tyr247 side chain of EB1-HD by hydrophobic interactions at the S2 site. Furthermore, the Lys493 main chain of the CLASP-rep1

peptide forms a hydrogen bond with the Arg222 side chain of EB1-HD. The residues of EB1-HD participating in interactions with CLASP are highly conserved among EB1 proteins (28) (Fig.II-3-4). The key residues of CLASP-rep1 for binding to EB1-HD are also highly conserved as the Ser-X-Ile-Pro motif among EB1 binding proteins and +TIPs containing the Ser/Arg/Lys rich region (48,49), which have been found in CLASP/Orbit/MAST (33,34), APC/Kar9 (50,51), MACF (28), Neuron navigator 1 (NAV1) (52), fibroblast growth factor receptor 1 oncogene partner (FOP1) (13), melanophilin (53), stromal interaction molecule 1 (STIM1) (54,55), mitotic centromere associated kinesin (MCAK) (56), *Drosophila* RhoGEF2 (57) and short stop 1 (28) (Fig.II-3-5).

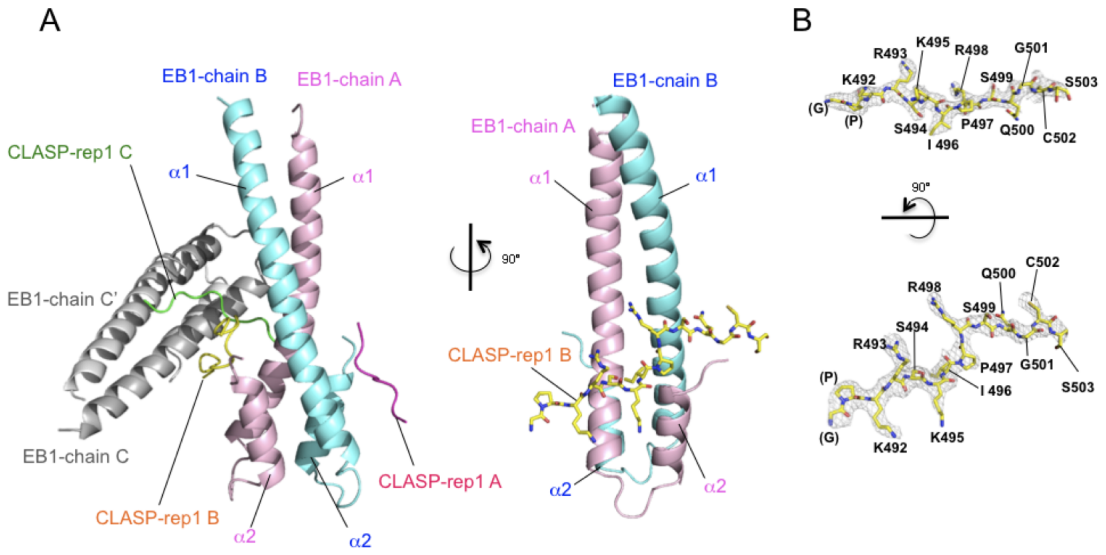

Fig. II-3-2. Crystal structure of EB1-CLASP complex.

A. *ribbon representations* of the EB1-HD complexed with the CLASP-rep1 peptide. *Left panel* shows that three EB1-HD molecules, EB1-chainA (pink), B (blue), C (gray), and three CLASP-rep1 peptides, CLASP-rep1 A(magenta), B (yerrow), C (green), are contained in asymmetric unit. EB1-chain C lies on two-fold axis of the crystallographic symmetry. The symmetric molecule of EB1-chain C is shown as EB1-chain C' (gray). One EB1-HD molecule contains two α-helixes, α1 and α2. EB1-chain A and B or C and C' are formed the coiled coil dimmer, respectively. *Right panel* represents a 90° rotation about the Y-axis. EB1-Chain C, C', CLASP-rep1 A and C is not shown to clarify for binding between CLASP-rep1 B and EB1-Chain A-B dimmer. CLASP-rep1 B is represented by the stick model.

B. *the stick model* of the CLASP-rep1 B bound EB1-chain A-B dimmer is shown in the omit electron density map for CLASP-rep1 B at the contour level of 1σ. Residue numbers of human CLASP2 are shown at the corresponding residues (labeled with *one-letter codes*) and N-terminal Gly-Pro residues that are a part of HRV3C protease recognition site are shown in parenthesis. *Upper panel* represents a 90° rotation about the x-axis.

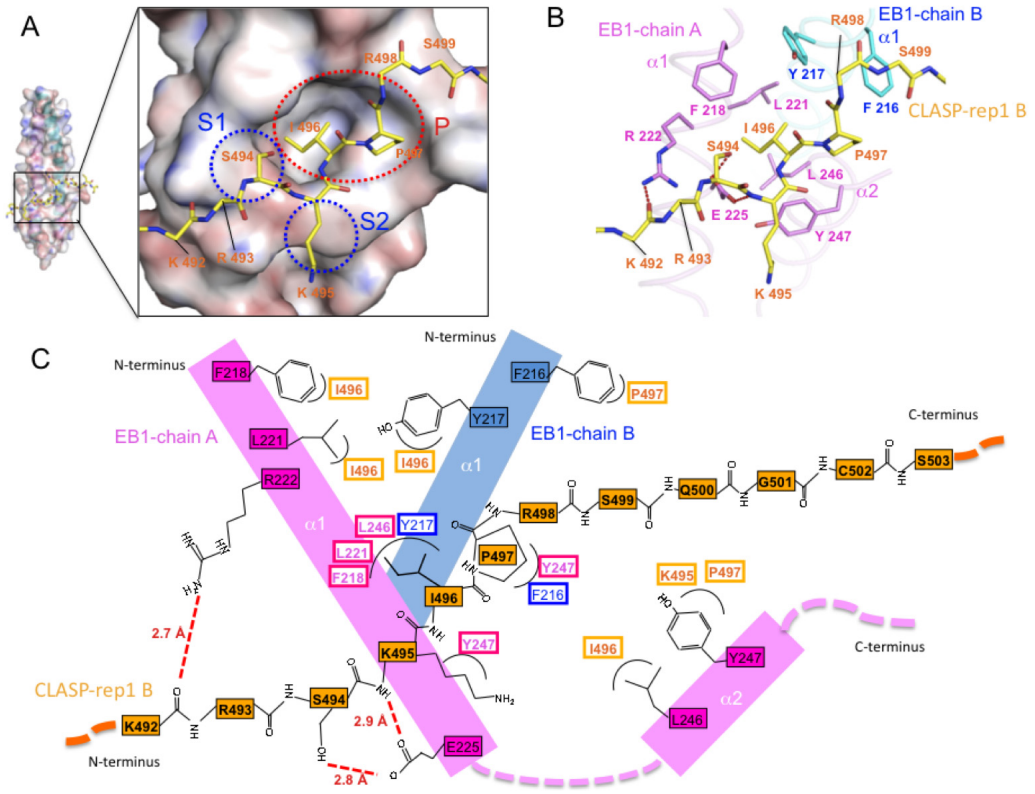

Fig. II-3-3. CLASP binding to the fore helix bundle region formed by EB1-HD dimmer.

A. the surface electrostatic potentials of the EB1-HD dimmer and a close-up view of the CLASP-rep1 peptide (*yellow stick model*) docked into the deep hydrophobic pocket formed by the fore helix bundle structure. The peptide is shown as a yellow *stick model* (labeled with *one-letter codes*). Two side chains of the binding sites (*S1 and S2*) bound the rim around a deep hydrophobic pocket are *labeled* and enclosed *blue circles*. The deep hydrophobic pocket (*P1*) is *labeled* and enclosed *a red circle*. The side chains of K492, R493, R498, Ser499 are not shown to clarify.

B. the close-up view of the CLASP-rep1 peptide (*yellow stick model*) binds the deep hydrophobic pocket formed by the fore helix bundle structure of EB1-HD dimmer. The side chains of EB1-chain A and B residues are shown as *pink* and *blue stick model*, respectively, while the main chains of EB1-chain A and B are shown as *ribbon model*. Hydrogen bonds formed within 3.2Å are shown as *red dashed lines*.

C. the schematic representation of the interactions between CLASP-rep1 peptide (*yerrow*) and EB1-HD dimmer (*pink and blue*). The nonpolar contacts involving side chains are shown with contacted residues. Hydrogen bonds formed within 3.2Å are shown as *red dashed lines*.

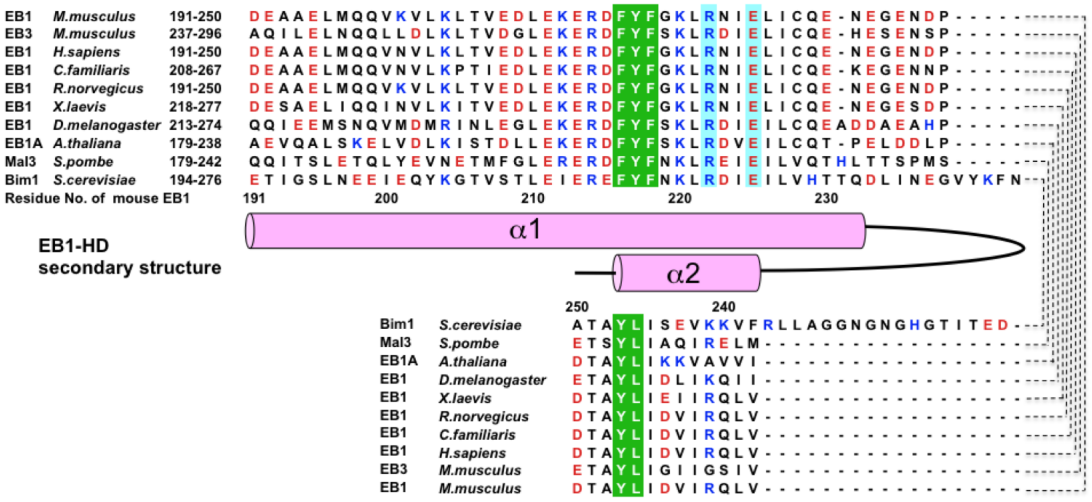

Fig. II-3-4. Sequence alignment of EB1 protein family.

The secondary structure of the mouse EB1-HD is shown at the *middle*. The two α-helix, α1 and α2, in an EB1-HD molecule are shown as *pink cylinders* and correspond with the sequence alignment. The basic and acidic residues are shown in *blue* and *red*, respectively. The residues that participate in nonpolar and polar residues interacting with the CLASP-rep1 peptide are *highlighted* in *green* and *blue boxes*, respectively.

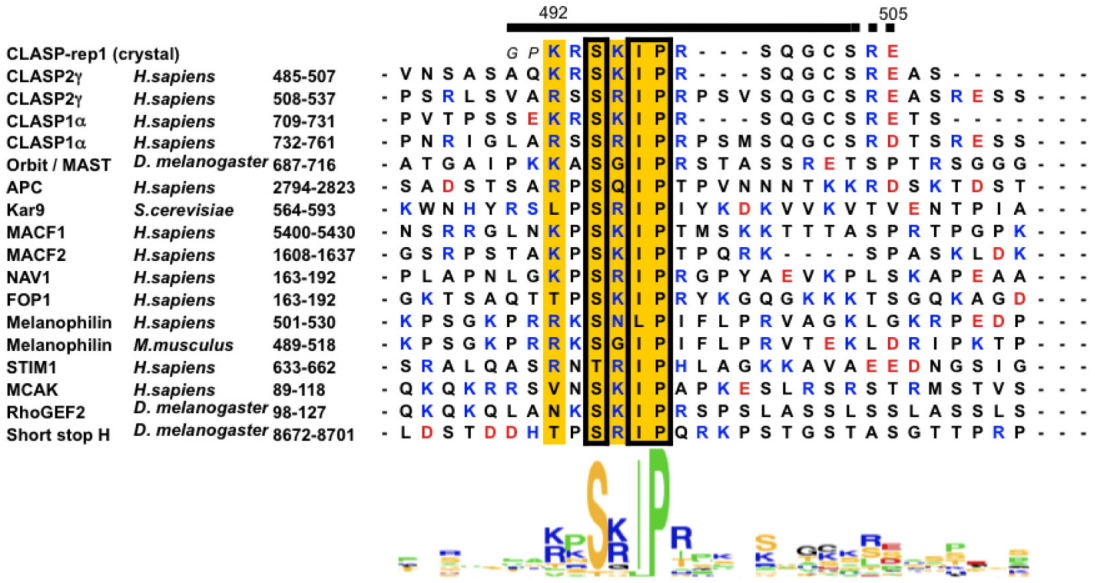

Fig. II-3-5. Sequence alignment of CLASP, EB1 binding proteins and other +TIPs

The alignment of the CLASP, EB1 binding proteins and Ser/Arg/Lys rich domain of other +TIPs containing Ser-X-Ile-Pro motif (15,48). The sequence of CLASP-rep1 used by the crystallization is shown at the *top* and N-terminal Gly-Pro residues are the parts of HRV3C recognition site. The *top line* shows that the *solid boldface lines* indicate CLASP-rep1 B peptide residues defined in the electron density maps, and the *dotted lines* indicate residues that were not defined in the electron density maps. The basic and acidic residues are shown in *blue* and *red*, respectively, and key residues for binding are marked with *boxes* and *highlighted* in *yellow*. The conserved residues are shown t*he bottom logo mark*. The logo mark was drawn by WebLogo (63).

II-4. Discussion

In this study, I have characterized CLASP-EB1 and CLASP-tubulin interactions and illustrated the precise binding mode of EB1 to CLASP using X-ray crystallography. The pull down assay in this study shows that CLASP encompasses two EB1-HD binding peptide regions (Fig. II-3-1 E and F). These peptide regions, CLASP-rep1 and CLASP-rep2, formed the tandem repeat sequence each other and contain Ser-Lys/Arg-Ile-Pro residues (see alignment in Fig. II-3-5). X-ray crystallography was successful to clarify that Ser-Lys-Ile-Pro residues in CLASP-rep1 are the key residues for binding to the hydrophobic pocket and its rim of the EB1-HD helix bundle structure (Fig.II-3-3 C). The main chain of Lys492 of CLASP-rep1 peptide forms a hydrogen bond with the side chain of Arg222 of EB1-HD. Hence, Lys492 of CLASP-rep1 might be less important for binding and indeed is poorly conserved among other +TIPs. Residues 499-505 in CLASP-rep1 B, which are located after the Ser-Lys-Ile-Pro sequence motif and less conserved among other +TIPs, have no significantly contacts with EB1-HD. In addition, residues 499-505 of CLASP-rep1 A and C were not observed in the electron density map. Residues 499-505 of CLASP-rep1 might be flexible and not necessarily participate in the direct interactions between EB1-HD and CLASP-rep1.

The pull down assay also shows that the CLASP Ser/Arg/Lys rich region contains tubulin binding sites. CLASP-rep1, which is only 14 residues, can bind to tubulin (Fig. II-3-1 F). The CLASP Ser/Arg/Lys rich region does not contain any CAP-Gly domain that is characterized with the conserved GKNDG motif for binding to the C-terminal end of EEY motif in tubulin (31). Thus, the tubulin binding activity

of the CLASP Ser/Arg/Lys region is comparatively similar to the APC basic domain (58), the GSR repeat in MACF (59) and tau (60,61). These Ser/Arg/Lys rich regions bind to the whole MT including the lattice and the ends probably by interaction with the tubulin and MT acidic surfaces through the positively charged residues Arg or Lys. CLASP can bind MT without CLIP-170 and strongly recruit EB1 to MT, which might be mediated with two EB1 binding repeats of CLASP (35). Interestingly, the tubulin binding region of CLASP overlaps the EB1-HD binding regions. The EB1-CLASP complex structure in this study shows that most side chains of basic residues are not involved in contacts with the EB1-HD dimmer. It is, therefore, possible that CLASP concurrently bind EB1 and tubulin at the Ser/Arg/Lys rich region. Thereby these two protein complexes are able to accumulate at MT plus ends to promote stabilization of MT plus ends and to stimulate polymerization of tubulins.

Recently, it has been reported that EB1-HD also associates with APC and MACF2, containing Ser-Lys/Gln-Ile-Pro residues in the Ser/Arg/Lys rich region (27,28). Mutation of Ile-pro residues of APC to alanine residues significantly reduced the binding affinity to EB1 (27). In addition, the interaction analysis between MACF2 and mutated EB1-HDindicates that the hydrophobic residues forming the hydrophobic pocket of EB1-HD are the key residues for interactions with MACF2 (28). These reports and the crystal structure in this study indicate that the Ser-X-Ile-Pro motif is the essential and general motif for binding to the EB1-HD hydrophobic pocket (48,49). Indeed, both EB1-HD residues necessary for association with CLASP-rep1 and the Ser-X-Ile-Pro motif are highly conserved among EB1 proteins and the Ser/Arg/Lys rich regions in +TIPs, respectively (Fig.II-3-4 and II-3-5). The fact implies that these +TIPs containing the Ser-X-Ile-Pro motif

competes with each other on binding to EB1 bound MT plus ends, which may increase the turnover of interactions between EB1 and +TIPs on MT plus ends. This may be related with the EB1 function that strongly promotes to recruit manifold +TIPs molecules to MT plus ends.

In conclusion, I performed the interaction analyses of EB1-CLASP and tubulin-CLASP interactions using pull down assay and showed that two tandem repeat regions in the CLASP Ser/Arg/Lys region binds the EB1-HD dimmer and the tubulin binding region of CLASP overlaps this EB1-HD binding regions. I speculate that CLASP/tubulin/EB1 complexes accumulate at MT plus ends and promote stabilization of MT plus ends and tubulin polymerization. The crystal structure investigation of the EB1-HD complexed with the CLASP-rep1 peptide reveals a CLASP peptide-binding mode to the EB1-HD dimmer distinct from the reported CLIP-binding model. Based on the current structure and reported EB1 binding regions of EB1 binding proteins, I suggest that the Ser-X-Ile-Pro motif is the essential and general motif for EB1-HD binding.

II-5. References

1). Desai, A., and Mitchison, T. J. (1997). Microtubule polymerization dynamics. *Annu Rev Cell Dev Biol* **13**, 83-117

2). Nogales, E., and Wang, H. W. (2006). Structural intermediates in microtubule assembly and disassembly: how and why? *Current Opinion in Cell Biology* **18**, 179-184

3). Schuyler, S. C., and Pellman, D. (2001). Microtubule "plus-end-tracking proteins": The end is just the beginning. *Cell* **105**, 421-424

4). Mimori-Kiyosue, Y., and Tsukita, S. (2003). "Search-and-capture" of microtubules through plus-end-binding proteins (+TIPs). *J Biochem* **134**, 321-326

5). Akhmanova, A., and Hoogenraad, C. C. (2005). Microtubule plus-end-tracking proteins: mechanisms and functions. *Curr Opin Cell Biol* **17**, 47-54

6). Xiang, X. (2006). A +TIP for a smooth trip. *J Cell Biol* **172**, 651-654

7). Su, L. K., Burrell, M., Hill, D. E., Gyuris, J., Brent, R., Wiltshire, R., Trent, J., Vogelstein, B., and Kinzler, K. W. (1995). APC binds to the novel protein EB1. *Cancer Res* **55**, 2972-2977

8). Nakamura, M., Zhou, X. Z., and Lu, K. P. (2001). Critical role for the EB1 and APC interaction in the regulation of microtubule polymerization. *Curr Biol* **11**, 1062-1067

9). Bieling, P., Laan, L., Schek, H., Munteanu, E. L., Sandblad, L., Dogterom, M., Brunner, D., and Surrey, T. (2007). Reconstitution of a microtubule plus-end tracking system in vitro. *Nature* **450**, 1100-1105

10). Mimori-Kiyosue, Y., Shiina, N., and Tsukita, S. (2000). The dynamic behavior of

the APC-binding protein EB1 on the distal ends of microtubules. *Curr Biol* **10**, 865-868

11). Berrueta, L., Kraeft, S. K., Tirnauer, J. S., Schuyler, S. C., Chen, L. B., Hill, D. E., Pellman, D., and Bierer, B. E. (1998). The adenomatous polyposis coli-binding protein EB1 is associated with cytoplasmic and spindle microtubules. *Proc Natl Acad Sci U S A* **95**, 10596-10601

12). Morrison, E. E., Wardleworth, B. N., Askham, J. M., Markham, A. F., and Meredith, D. M. (1998). EB1, a protein which interacts with the APC tumour suppressor, is associated with the microtubule cytoskeleton throughout the cell cycle. *Oncogene* **17**, 3471-3477

13). Yan, X., Habedanck, R., and Nigg, E. A. (2006). A complex of two centrosomal proteins, CAP350 and FOP, cooperates with EB1 in microtubule anchoring. *Mol Biol Cell* **17**, 634-644

14). Vaughan, K. T. (2005). TIP maker and TIP marker; EB1 as a master controller of microtubule plus ends. *J Cell Biol* **171**, 197-200

15). Akhmanova, A., and Steinmetz, M. O. (2008). Tracking the ends: a dynamic protein network controls the fate of microtubule tips. *Nat Rev Mol Cell Biol* **9**, 309-322

16). Dixit, R., Barnett, B., Lazarus, J. E., Tokito, M., Goldman, Y. E., and Holzbaur, E. L. (2009). Microtubule plus-end tracking by CLIP-170 requires EB1. *Proc Natl Acad Sci U S A*

17). Lansbergen, G., and Akhmanova, A. (2006). Microtubule plus end: a hub of cellular activities. *Traffic* **7**, 499-507

18). Vitre, B., Coquelle, F. M., Heichette, C., Garnier, C., Chretien, D., and Arnal, I.

(2008). EB1 regulates microtubule dynamics and tubulin sheet closure in vitro. *Nat Cell Biol* **10**, 415-421

19). Wittmann, T. (2008). EBs clip CLIPs to growing microtubule ends. *J Cell Biol* **183**, 1183-1185

20). Bieling, P., Kandels-Lewis, S., Telley, I. A., van Dijk, J., Janke, C., and Surrey, T. (2008). CLIP-170 tracks growing microtubule ends by dynamically recognizing composite EB1/tubulin-binding sites. *J Cell Biol* **183**, 1223-1233

21). des Georges, A., Katsuki, M., Drummond, D. R., Osei, M., Cross, R. A., and Amos, L. A. (2008). Mal3, the Schizosaccharomyces pombe homolog of EB1, changes the microtubule lattice. *Nat Struct Mol Biol* **15**, 1102-1108

22). Hayashi, I., and Ikura, M. (2003). Crystal structure of the amino-terminal microtubule-binding domain of end-binding protein 1 (EB1). *J Biol Chem* **278**, 36430-36434

23). Gimona, M., Djinovic-Carugo, K., Kranewitter, W. J., and Winder, S. J. (2002). Functional plasticity of CH domains. *FEBS Lett* **513**, 98-106

24). Sjoblom, B., Ylanne, J., and Djinovic-Carugo, K. (2008). Novel structural insights into F-actin-binding and novel functions of calponin homology domains. *Curr Opin Struct Biol* **18**, 702-708

25). Kodama, A., Karakesisoglou, I., Wong, E., Vaezi, A., and Fuchs, E. (2003). ACF7: an essential integrator of microtubule dynamics. *Cell* **115**, 343-354

26). Sun, D., Leung, C. L., and Liem, R. K. (2001). Characterization of the microtubule binding domain of microtubule actin crosslinking factor (MACF): identification of a novel group of microtubule associated proteins. *J Cell Sci* **114**, 161-172

27). Honnappa, S., John, C. M., Kostrewa, D., Winkler, F. K., and Steinmetz, M. O. (2005). Structural insights into the EB1-APC interaction. *EMBO J* **24**, 261-269

28). Slep, K. C., Rogers, S. L., Elliott, S. L., Ohkura, H., Kolodziej, P. A., and Vale, R. D. (2005). Structural determinants for EB1-mediated recruitment of APC and spectraplakins to the microtubule plus end. *J Cell Biol* **168**, 587-598

29). Wen, Y., Eng, C. H., Schmoranzer, J., Cabrera-Poch, N., Morris, E. J., Chen, M., Wallar, B. J., Alberts, A. S., and Gundersen, G. G. (2004). EB1 and APC bind to mDia to stabilize microtubules downstream of Rho and promote cell migration. *Nat Cell Biol* **6**, 820-830

30). Hayashi, I., Wilde, A., Mal, T. K., and Ikura, M. (2005). Structural basis for the activation of microtubule assembly by the EB1 and p150Glued complex. *Mol Cell* **19**, 449-460

31). Mishima, M., Maesaki, R., Kasa, M., Watanabe, T., Fukata, M., Kaibuchi, K., and Hakoshima, T. (2007). Structural basis for tubulin recognition by cytoplasmic linker protein 170 and its autoinhibition. *Proc Natl Acad Sci U S A* **104**, 10346-10351

32). Akhmanova, A., Hoogenraad, C. C., Drabek, K., Stepanova, T., Dortland, B., Verkerk, T., Vermeulen, W., Burgering, B. M., De Zeeuw, C. I., Grosveld, F., and Galjart, N. (2001). Clasps are CLIP-115 and -170 associating proteins involved in the regional regulation of microtubule dynamics in motile fibroblasts. *Cell* **104**, 923-935

33). Inoue, Y. H., do Carmo Avides, M., Shiraki, M., Deak, P., Yamaguchi, M., Nishimoto, Y., Matsukage, A., and Glover, D. M. (2000). Orbit, a novel microtubule-associated protein essential for mitosis in Drosophila melanogaster. *J Cell Biol* **149**, 153-166

34). Lemos, C. L., Sampaio, P., Maiato, H., Costa, M., Omel'yanchuk, L. V., Liberal,

V., and Sunkel, C. E. (2000). Mast, a conserved microtubule-associated protein required for bipolar mitotic spindle organization. *EMBO J* **19**, 3668-3682

35). Mimori-Kiyosue, Y., Grigoriev, I., Lansbergen, G., Sasaki, H., Matsui, C., Severin, F., Galjart, N., Grosveld, F., Vorobjev, I., Tsukita, S., and Akhmanova, A. (2005). CLASP1 and CLASP2 bind to EB1 and regulate microtubule plus-end dynamics at the cell cortex. *J Cell Biol* **168**, 141-153

36). Lansbergen, G., Grigoriev, I., Mimori-Kiyosue, Y., Ohtsuka, T., Higa, S., Kitajima, I., Demmers, J., Galjart, N., Houtsmuller, A. B., Grosveld, F., and Akhmanova, A. (2006). CLASPs attach microtubule plus ends to the cell cortex through a complex with LL5 beta. *Developmental Cell* **11**, 21-32

37). Sandblad, L., Busch, K. E., Tittmann, P., Gross, H., Brunner, D., and Hoenger, A. (2006). The Schizosaccharomyces pombe EB1 homolog Mal3p binds and stabilizes the microtubule lattice seam. *Cell* **127**, 1415-1424

38). Kikkawa, M., and Metlagel, Z. (2006). A molecular "zipper" for microtubules. *Cell* **127**, 1302-1304

39). Otwinowski, Z., and Minor, W. (1997). Processing of X-ray diffraction data collected in oscillation mode. *Macromolecular Crystallography, Pt A* **276**, 307-326

40). Vonrhein, C., Blanc, E., Roversi, P., and Bricogne, G. (2007). Automated structure solution with autoSHARP. *Methods Mol Biol* **364**, 215-230

41). Emsley, P., and Cowtan, K. (2004). Coot: model-building tools for molecular graphics. *Acta Crystallogr D Biol Crystallogr* **60**, 2126-2132

42). Vagin, A. A., Steiner, R. A., Lebedev, A. A., Potterton, L., McNicholas, S., Long, F., and Murshudov, G. N. (2004). REFMAC5 dictionary: organization of prior chemical knowledge and guidelines for its use. *Acta Crystallogr D Biol Crystallogr*

60, 2184-2195

43). Brunger, A. T., Adams, P. D., Clore, G. M., DeLano, W. L., Gros, P., Grosse-Kunstleve, R. W., Jiang, J. S., Kuszewski, J., Nilges, M., Pannu, N. S., Read, R. J., Rice, L. M., Simonson, T., and Warren, G. L. (1998). Crystallography & NMR system: A new software suite for macromolecular structure determination. *Acta Crystallogr D Biol Crystallogr* **54**, 905-921

44). Davis, I. W., Leaver-Fay, A., Chen, V. B., Block, J. N., Kapral, G. J., Wang, X., Murray, L. W., Arendall, W. B., 3rd, Snoeyink, J., Richardson, J. S., and Richardson, D. C. (2007). MolProbity: all-atom contacts and structure validation for proteins and nucleic acids. *Nucleic Acids Res* **35**, W375-383

45). Davis, I. W., Murray, L. W., Richardson, J. S., and Richardson, D. C. (2004). MOLPROBITY: structure validation and all-atom contact analysis for nucleic acids and their complexes. *Nucleic Acids Res* **32**, W615-619

46). Baker, N. A., Sept, D., Joseph, S., Holst, M. J., and McCammon, J. A. (2001). Electrostatics of nanosystems: application to microtubules and the ribosome. *Proc Natl Acad Sci U S A* **98**, 10037-10041

47). Holst, M., Baker, N., and Wang, F. (2000). Adaptive multilevel finite element solution of the Poisson-Boltzmann equation I. Algorithms and examples. *Journal of Computational Chemistry* **21**, 1319-1342

48). Neduva, V., and Russell, R. B. (2006). DILIMOT: discovery of linear motifs in proteins. *Nucleic Acids Res* **34**, W350-355

49). Galjart, N. (2005). CLIPs and CLASPs and cellular dynamics. *Nat Rev Mol Cell Biol* **6**, 487-498

50). Miller, R. K., and Rose, M. D. (1998). Kar9p is a novel cortical protein required

for cytoplasmic microtubule orientation in yeast. *Journal of Cell Biology* **140**, 377-390

51). Korinek, W. S., Copeland, M. J., Chaudhuri, A., and Chant, J. (2000). Molecular linkage underlying microtubule orientation toward cortical sites in yeast. *Science* **287**, 2257-2259

52). Martinez-Lopez, M. J., Alcantara, S., Mascaro, C., Perez-Branguli, F., Ruiz-Lozano, P., Maes, T., Soriano, E., and Buesa, C. (2005). Mouse neuron navigator 1, a novel microtubule-associated protein involved in neuronal migration. *Mol Cell Neurosci* **28**, 599-612

53). Wu, X. S., Tsan, G. L., and Hammer, J. A., 3rd. (2005). Melanophilin and myosin Va track the microtubule plus end on EB1. *J Cell Biol* **171**, 201-207

54). Jermy, A. (2008). STIM1 tracks growing microtubule ends. *Nat Cell Biol* **10**, 384

55). Grigoriev, I., Gouveia, S. M., van der Vaart, B., Demmers, J., Smyth, J. T., Honnappa, S., Splinter, D., Steinmetz, M. O., Putney, J. W., Jr., Hoogenraad, C. C., and Akhmanova, A. (2008). STIM1 is a MT-plus-end-tracking protein involved in remodeling of the ER. *Curr Biol* **18**, 177-182

56). Lee, T., Langford, K. J., Askham, J. M., Bruning-Richardson, A., and Morrison, E. E. (2008). MCAK associates with EB1. *Oncogene* **27**, 2494-2500

57). Rogers, S. L., Wiedemann, U., Hacker, U., Turck, C., and Vale, R. D. (2004). Drosophila RhoGEF2 associates with microtubule plus ends in an EB1-dependent manner. *Curr Biol* **14**, 1827-1833

58). Deka, J., Kuhlmann, J., and Muller, O. (1998). A domain within the tumor suppressor protein APC shows very similar biochemical properties as the microtubule-associated protein tau. *Eur J Biochem* **253**, 591-597

59). Sun, D. M., Leung, C. L., and Liem, R. K. H. (2001). Characterization of the microtubule binding domain of microtubule actin crosslinking factor (MACF): identification of a novel group of microtubule associated proteins. *Journal of Cell Science* **114**, 161-172

60). Weingarten, M. D., Lockwood, A. H., Hwo, S. Y., and Kirschner, M. W. (1975). A protein factor essential for microtubule assembly. *Proc Natl Acad Sci U S A* **72**, 1858-1862

61). Dehmelt, L., and Halpain, S. (2005). The MAP2/Tau family of microtubule-associated proteins. *Genome Biol* **6**, 204

62). Hayashi, I., Plevin, M. J., and Ikura, M. (2007). CLIP170 autoinhibition mimics intermolecular interactions with p150Glued or EB1. *Nat Struct Mol Biol* **14**, 980-981

63). Crooks, G. E., Hon, G., Chandonia, J. M., and Brenner, S. E. (2004). WebLogo: a sequence logo generator. *Genome Res* **14**, 1188-1190

III. Acknowledgments

This present studies have been performed under the direction of Dr. Toshio Hakoshima (Graduate School of Information Sciences, Nara Institute of Science and Technology). I would like to express my gratitude to him for his guidance and discussions throughout all my studies. I also would like to thank Drs. Tatuo Takeya, Hiroshi Itoh, and Chojiro Kojima (Graduate School of Biological Sciences, Nara Institute of Science and Technology) for their practical advices and helpful discussion for my studies.

I gratefully acknowledge Dr. Sachiko Tsukita and Dr. Shoichiro Tsukita (Department of Cell Biology, Faculty of Medicine, Kyoto university) for providing the mouse radixin, the mouse CD44 and the mouse EB1 cDNA.

I gratefully acknowledge Dr. Kozo Kaibuchi (Department of Cell Pharmacology, Faculty of Medicine, Nagoya university) for providing the human CLASP1α and 2γ cDNA.

I would like to thank K. Hasegawa, H. Sakai and M. Yamamoto at SPring-8 for help with data collection at synchrotron beamline BL38B1. I would like to thank J. Tsukamoto (Graduate School of Biological Sciences, Nara Institute of Science and Technology) for technical support in performing the matrix-assisted laser desorption/ionization time-off light mass spectroscopy analysis.

I would like to thank Dr. Ken Kitano for help with data collection, structure analysis.

I also would like to thank Drs. Ryoko Mishima-Maesaki, Sigeru Sakurai, Terawaki Shinichi and Ms. Yayoi Fukami for advices of the protein purification and the crystallization method. Finally, I would like to thank all members of Dr. Toshio Hakoshima's group and Dr. Chojiro Kojima's group. I could perform my all experiments comfortably. I would like to appreciate their kindness.

Tomoyuki Mori